

Detection of amino acetonitrile in Sgr B2(N) [★]

A. Belloche¹, K. M. Menten¹, C. Comito¹, H. S. P. Müller^{1,2}, P. Schilke¹, J. Ott^{3,4}, S. Thorwirth¹, and C. Hieret¹

¹ Max-Planck Institut für Radioastronomie, Auf dem Hügel 69, D-53121 Bonn, Germany
e-mail: belloche, kmenten, ccomito, schilke, sthorwirth, chieret@mpi.fr-bonn.mpg.de

² I. Physikalisches Institut, Universität zu Köln, Zùlpicher Str. 77, D-50937 Köln, Germany
e-mail: hspm@ph1.uni-koeln.de

³ CSIRO Australia Telescope National Facility, Cnr Vimiera & Pembroke Roads, Marsfield NSW 2122, Australia

⁴ National Radio Astronomy Observatory, 520 Edgemont Road, Charlottesville, VA 22903-2475, USA
e-mail: jott@nrao.edu

Received 6 December 2007; accepted 16 January 2008

ABSTRACT

Context. Amino acids are building blocks of proteins and therefore key ingredients for the origin of life. The simplest amino acid, glycine (NH₂CH₂COOH), has long been searched for in the interstellar medium but has not been unambiguously detected so far. At the same time, more and more complex molecules have been newly found toward the prolific Galactic center source Sagittarius B2.

Aims. Since the search for glycine has turned out to be extremely difficult, we aimed at detecting a chemically related species (possibly a direct precursor), amino acetonitrile (NH₂CH₂CN).

Methods. With the IRAM 30m telescope we carried out a complete line survey of the hot core regions Sgr B2(N) and (M) in the 3 mm range, plus partial surveys at 2 and 1.3 mm. We analyzed our 30m line survey in the LTE approximation and modeled the emission of all known molecules simultaneously. We identified spectral features at the frequencies predicted for amino acetonitrile lines having intensities compatible with a unique rotation temperature. We also used the Very Large Array to look for cold, extended emission from amino acetonitrile.

Results. We detected amino acetonitrile in Sgr B2(N) in our 30m telescope line survey and conducted confirmatory observations of selected lines with the IRAM Plateau de Bure and the Australia Telescope Compact Array interferometers. The emission arises from a known hot core, the Large Molecule Heimat, and is compact with a source diameter of 2'' (0.08 pc). We derived a column density of 2.8×10^{16} cm⁻², a temperature of 100 K, and a linewidth of 7 km s⁻¹. Based on the simultaneously observed continuum emission, we calculated a density of 1.7×10^8 cm⁻³, a mass of 2340 M_⊙, and an amino acetonitrile fractional abundance of 2.2×10^{-9} . The high abundance and temperature may indicate that amino acetonitrile is formed by grain surface chemistry. We did not detect any hot, compact amino acetonitrile emission toward Sgr B2(M) or any cold, extended emission toward Sgr B2, with column-density upper limits of 6×10^{15} and $3 \times 10^{12-14}$ cm⁻², respectively.

Conclusions. Based on our amino acetonitrile detection toward Sgr B2(N) and a comparison to the pair methylcyanide/acetic acid both detected in this source, we suggest that the column density of both glycine conformers in Sgr B2(N) is well below the best upper limits published recently by other authors, and probably below the confusion limit in the 1-3 mm range.

Key words. Astrobiology – Astrochemistry – Line: identification – Stars: formation – ISM: individual objects: Sagittarius B2 – ISM: molecules

1. Introduction – general methods

Among the still growing list of complex molecules found in the interstellar medium, so-called “bio”molecules garner special attention. In particular, the quest for interstellar amino acids, building blocks of proteins, has engaged radio and millimeter wavelength astronomers for a long time. Numerous published and unpublished searches have been made for interstellar glycine, the simplest amino acid (Brown et al. 1979; Hollis et al. 1980; Berulis et al. 1985; Combes et al 1996; Ceccarelli et al. 2000;

Hollis et al. 2003; Jones et al. 2007; Cunningham et al. 2007). Its recent “detection” claimed by Kuan et al. (2003) has been persuasively rebutted by Snyder et al. (2005). Since the early days of molecular radio astronomy, Sagittarius B2 has been a favorite target in searches for complex molecules in space.

1.1. The target: Sagittarius B2

Sagittarius B2 (hereafter Sgr B2 for short) is a very massive (several million solar masses) and extremely active region of high-mass star formation at a projected distance of ~ 100 pc from the Galactic center. Its distance from the Sun is assumed to be the same as the Galactic center distance, R_0 . Reid (1993), reviewing various methods to determine R_0 , arrived at a “best estimate” of 8.0 ± 0.5 kpc, a value that we adopt in this article. It is supported by recent modeling of trajectories of stars orbiting the central black hole, which yields 7.94 ± 0.42 kpc (Eisenhauer et al. 2003).

Send offprint requests to: A. Belloche

[★] Based on observations carried out with the IRAM Plateau de Bure Interferometer, the IRAM 30m telescope, the Australia Telescope Compact Array, and the NRAO Very Large Array. IRAM is supported by INSU/CNRS (France), MPG (Germany) and IGN (Spain). The Australia Telescope Compact Array is part of the Australia Telescope which is funded by the Commonwealth of Australia for operation as a National Facility managed by CSIRO. The National Radio Astronomy Observatory is a facility of the National Science Foundation operated under cooperative agreement by Associated Universities, Inc.

There are two major centers of activity, Sgr B2(M) and Sgr B2(N) separated by ~ 2 pc. In each of them, recent star formation manifests itself in a multitude of HII regions of many sizes, from hypercompact to compact (Gaume et al. 1995), and there is abundant material to form new stars evident by massive sources of molecular line and submillimeter continuum emission from dust (Lis et al. 1991, 1993).

1.1.1. Sgr B2 as part of the Central Molecular Zone

Some of the first detections of interstellar organic molecules (at cm-wavelengths!) were made toward Sgr B2 (see Menten 2004 for a historical perspective). The low intrinsic line strengths make these cm lines unlikely candidates for detection. However, the situation is helped, first, by the fact that many of the transitions in question may have inverted levels (Menten 2004) and amplify background radio continuum emission which is very intense at cm wavelengths (Hollis et al. 2007). Second, the spatial distributions of many species are characterized by spatially extended emission covering areas beyond Sgr B2 itself, filling single dish telescope beams, thus producing appreciable intensity even when observed with low spatial resolution (Cummins, Linke, & Thaddeus 1986; Jones et al., *in prep.*). This emission is characterized by low rotation temperatures, favoring lower frequency lines. Recent identifications of “new” species include glycolaldehyde CH_2OHCHO (Hollis et al. 2000, 2001), ethylene glycol $\text{HOCH}_2\text{CH}_2\text{OH}$ (Hollis et al. 2002), and vinyl alcohol CH_2CHOH (Turner & Apponi 2001).

Sgr B2 and its surroundings are part of the Central Molecular Zone (CMZ) of our Galaxy, a $\sim \pm 0.3$ latitude wide band stretching around the Galactic center from longitude $l \sim +1^\circ.6$ to $-1^\circ.1$ (see, e.g., Morris & Serabyn 1996). The CMZ contains spatially extended emission of many complex organic molecules (Minh et al. 1992; Dahmen et al. 1997; Menten 2004; Requena-Torres et al. 2006).

1.1.2. The Large Molecule Heimat

Near Sgr B2(N), there is a hot, dense compact source that has a mm-wavelength line density second to no other known object. This source, for which Snyder, Kuan, & Miao (1994) coined the name “Large Molecule Heimat” (LMH), is characterized by very high densities ($> 10^7 \text{ cm}^{-3}$) and gas temperatures ($> 100 \text{ K}$). In recent years arcsecond resolution interferometry with the BIMA array has resulted in the detection and imaging of increasingly complex organic species toward the LMH, such as vinyl cyanide CH_2CHCN , methyl formate HCOOCH_3 , and ethyl cyanide $\text{CH}_3\text{CH}_2\text{CN}$ (Miao et al. 1995; Miao & Snyder 1997), formamide NH_2CHO , isocyanic acid HNCO , and methyl formate HCOOCH_3 (Kuan & Snyder 1996), acetic acid CH_3COOH (Mehringer et al. 1997; Remijan et al. 2002), formic acid HCOOH (Liu et al. 2001), and acetone $(\text{CH}_3)_2\text{CO}$ (Snyder et al. 2002). All the interferometric observations are consistent with a compact ($< \text{few arcsec}$ diameter) source that had already been identified as the source of high-density-tracing non-metastable ammonia line emission by Vogel et al. (1987) and thermal methanol emission by Mehringer & Menten (1997, their source “i”). The LMH also hosts a powerful H_2O maser region (Reid et al. 1988), which provides evidence that it is very young (see Sect. 4.1).

1.2. The complex spectra of complex molecules

Complex molecules in general have large partition functions, in particular for the elevated temperatures ($> 100 \text{ K}$) in molecular hot cores, dense and compact cloud condensations internally heated by a deeply embedded, young high-mass (proto)stellar object. Therefore, most individual spectral lines are weak and might easily get hidden in the “line forest” found toward these frequently extremely line-rich sources. To a large part, this forest consists of rotational lines, many of them presently unidentifiable, from within relatively low-lying vibrational states of molecules. Most of the candidate molecules from which these lines originate are known to exist in these sources, but laboratory spectroscopy is presently lacking for lines from the states in question. At this point in the game, unequivocally identifying a species in a spectrum of a hot core covering a wide spectral range requires the following steps: as described in detail in Sect. 3.2, assuming Local Thermodynamic Equilibrium (LTE) (which applies at the high densities in hot cores) a model spectrum is calculated for an assumed rotation temperature, column density, line width and other parameters. This predicts lines of a given intensity at all the known frequencies. Then at least two conditions have to be fulfilled: (i) All predicted lines should have a counterpart in the observed spectrum with the right intensity and width – no single line should be missing. (ii) Follow-up observations with interferometers have to prove whether all lines from the candidate species are emitted from the same spot. Given the chemical variety in hot core regions, this is a powerful constraint. Moreover, interferometer images tend to have less line confusion, since many lines that are blended in larger beam single-dish spectra arise from different locations or are emitted by an extended region that is spatially filtered out. Using an interferometer for aiding molecule identifications was pioneered by L. Snyder and collaborators who (mostly) used the Berkeley-Illinois-Maryland-Array (BIMA) to clearly identify a number of species in the Sgr B2(N) Large Molecule Heimat (see Sect. 1.1.2).

We carried out a complete line survey of the hot core regions Sgr B2(N) and (M) with the IRAM 30m telescope at 3 mm, along with partial surveys at 2 and 1.3 mm. One of the overall goals of our survey was to better characterize the molecular content of both regions. It also allows searches for “new” species once we have identified the lines emitted by known molecules (including vibrationally and torsionally excited states). In particular, many complex molecules have enough lines in the covered frequency ranges to apply criterion (i) above. Once a species fulfils this criterion, interferometer measurements of selected lines can be made to check criterion (ii).

1.3. Amino acetonitrile

One of our target molecules was amino acetonitrile ($\text{NH}_2\text{CH}_2\text{CN}$), a molecule chemically related to glycine. Whether it is a precursor to the latter is under debate (see Sect. 4.3). Not many astronomical searches for amino acetonitrile have been reported in the literature. In his dissertation, Storey (1976) reported searches for the $J_{K_a, K_c} = 2_{11} - 2_{12}$ and $1_{01} - 0_{00}$ transitions at 1350.5 and 9071.7 MHz, respectively with the Parkes 64 m telescope. On afterthought, the only chance of success for their observations would have been if amino acetonitrile existed on large spatial scales, similar to the molecules described in Sect. 1.1.1 (see Sect. 3.7 for further limits on extended amino acetonitrile emission). Recently, Wirström et al. (2007) reported unsuccessful searches of a

number of mm-wavelength transitions of amino acetonitrile toward a number of hot cores.

Here, we report our detection of warm compact emission from amino acetonitrile in Sgr B2(N) with the IRAM 30m telescope, the Plateau de Bure Interferometer (PdBI) and the Australia Telescope Compact Array (ATCA), and upper limits on cold, spatially extended emission from amino acetonitrile that we obtained with the NRAO Very Large Array (VLA). Section 2 summarizes the observational details. We present our results in Sect. 3. Implications in terms of interstellar chemistry are discussed in Sect. 4. Our conclusions are summarized in Sect. 5.

2. Observations and data reduction

2.1. Single-dish observations and data reduction

We carried out millimeter line observations with the IRAM 30m telescope on Pico Veleta, Spain, in January 2004, September 2004 and January 2005. We used four SIS heterodyne receivers simultaneously, two in the 3 mm window connected to the autocorrelation spectrometer VESPA and two in the 1.3 mm window with filter banks as backends. A few selected frequency ranges were also observed with one SIS receiver at 2 mm in January 2004. The channel spacing and bandwidth were 0.313 and 420 MHz for each receiver at 3 and 2 mm, and 1 and 512 MHz for each receiver at 1.3 mm, respectively. The observations were done in single-sideband mode with sideband rejections of $\sim 1\text{--}3\%$ at 3 mm, $\sim 5\text{--}7\%$ at 2 mm, and $\sim 5\text{--}8\%$ at 1.3 mm. The half-power beamwidths can be computed with the equation $\text{HPBW} (") = \frac{2460}{\nu(\text{GHz})}$. The forward efficiencies F_{eff} were 0.95 at 3 mm, 0.93 at 2 mm, and 0.91 at 1.3 mm, respectively. The main-beam efficiencies were computed using the Ruze function $B_{\text{eff}} = 1.2\epsilon e^{-(4\pi R\sigma/\lambda)^2}$, with $\epsilon = 0.69$, $R\sigma = 0.07$, and λ the wavelength in mm (see the IRAM 30m telescope system summary on <http://www.iram.es>). The system temperatures ranged from 96 to 600 K at 3 mm, from 220 to 720 K at 2 mm (except at 176 GHz where they ranged from 2400 to 3000 K), and from 280 to 1200 K at 1.3 mm. The telescope pointing was checked every ~ 1.5 hours on Mercury, Mars, 1757–240 or G10.62, and found to be accurate to 2–3" (rms). The telescope focus was optimized on Mercury, Jupiter, Mars or G34.3+0.2 every $\sim 1.5\text{--}3$ hours. The observations were performed toward both sources Sgr B2(N) ($\alpha_{\text{J2000}}=17^{\text{h}}47^{\text{m}}20^{\text{s}}.0$, $\delta_{\text{J2000}}=-28^{\circ}22'19.0''$, $V_{\text{lsr}} = 64 \text{ km s}^{-1}$) and Sgr B2(M) ($\alpha_{\text{J2000}}=17^{\text{h}}47^{\text{m}}20^{\text{s}}.4$, $\delta_{\text{J2000}}=-28^{\circ}23'07.0''$, $V_{\text{lsr}} = 62 \text{ km s}^{-1}$) in position-switching mode with a reference position offset by $(\Delta\alpha, \Delta\delta)=(-752'', +342'')$ with respect to the former. The emission toward this reference position was found to be weak: $T_{\text{a}}^*(^{12}\text{CO } 1\text{--}0) \sim 2 \text{ K}$, $T_{\text{a}}^*(\text{CS } 2\text{--}1) \leq 0.05 \text{ K}$, $T_{\text{a}}^*(^{12}\text{CO } 2\text{--}1) \sim 1.5 \text{ K}$, $T_{\text{a}}^*(^{13}\text{CO } 2\text{--}1) \lesssim 0.1 \text{ K}$, and it is negligible for higher excitation lines and/or complex species.

We observed the full 3 mm window between 80 and 116 GHz toward both sources. The step between two adjacent tuning frequencies was 395 MHz, which yielded an overlap of 50 MHz. The autocorrelator VESPA produces artificial spikes with a width of 3–5 channels at the junction between subbands (typically 2 or 3 spikes per spectrum). To get rid of these artefacts, half of the integration time at each tuning frequency was spent with the backend shifted by 50 MHz, so that we could, without any loss of information, systematically remove in each spectrum 5 channels at each of the 6 junctions between subbands that were possibly affected by this phenomenon. At 2 mm, we observed at only 8 selected frequencies, and removed the artificial spikes in the same way as at 3 mm. At 1 mm, we covered the frequency

ranges 201.8 to 204.6 GHz and 205.0 to 217.7 GHz, plus a number of selected spots at higher frequency. For each individual spectrum, we removed a 0th-order (constant) baseline by selecting a group of channels which seemed to be free of emission or absorption. However, many spectra are full of lines, especially at 1.3 mm where we reached the confusion limit, and we may have overestimated the level of the baseline for some of them.

In T_{a}^* scale, the rms noise level achieved towards Sgr B2(N) is about 15–20 mK below 100 GHz, 20–30 mK between 100 and 114.5 GHz, and about 50 mK between 114.5 and 116 GHz. At 1.3 mm, we reached the confusion limit for most of the spectra. The data were reduced with the CLASS software, which is part of the GILDAS software package (see <http://www.iram.fr/IRAMFR/GILDAS>).

2.2. Interferometric observations with the PdBI

We observed Sgr B2(N) with the PdBI for 4.7 hours on February 7th, 2006 with 6 antennas in the high-resolution A configuration (E24E68E04N46W27N29). The coordinates of the phase center were $\alpha_{\text{J2000}} = 17^{\text{h}}47^{\text{m}}20^{\text{s}}.00$, $\delta_{\text{J2000}} = -28^{\circ}22'19.0''$. The 3 and 1.2 mm receivers were tuned to 81.982 and 245.380 GHz, respectively, in single side band mode. At 3 mm, there were two spectral windows centered at 81.736 and 82.228 GHz with a bandwidth of 80 MHz and a channel separation of 0.313 MHz, and two continuum windows of 320 MHz bandwidth centered at 81.852 and 82.112 GHz. The atmospheric phase stability was good for the 3 mm band but bad for the 1.2 mm band. Therefore we do not analyze the 1.2 mm data. The system temperatures were typically 150–220 K at 3 mm in the lower sideband. The (naturally-weighted) synthesized half-power beam width was $3.4'' \times 0.8''$ with P.A. 10° , and the primary beam was $\sim 61''$ FWHM. The correlator bandpass was calibrated on the quasar 3C 273. Phase calibration was determined on the nearby sources NRAO 530 and 1622–297. The time-dependent amplitude calibration was done on 1622–297, NRAO 530, 1334–127, and 1749+096, while the absolute flux density scale was derived from MWC 349. The absolute calibration uncertainty is estimated to be $\sim 15\%$. The data were calibrated and imaged using the GILDAS software. The continuum emission was estimated on line-free portions of the bands and removed in the uv plane. The deconvolution was performed with the CLEAN method (Clark 1980).

2.3. Interferometric observations with the ATCA

We observed Sgr B2(N) with the ATCA on May 17th, 2006 in the hybrid H 214 configuration for 6 hours, for 7 hours on July 30th, 2006 in the H 168 configuration, and for 6 hours in the compact H 75 configuration on September 25th, 2006. The coordinates of the phase center were $\alpha_{\text{J2000}} = 17^{\text{h}}47^{\text{m}}20^{\text{s}}.00$, $\delta_{\text{J2000}} = -28^{\circ}22'19.0''$. The 3 mm receiver was alternately tuned to three frequency pairs of 90.550 and 93.200 GHz, 90.779 and 93.200 GHz, and 99.978 and 97.378 GHz in single side band mode, where only the first frequency of each pair was in spectral line mode with 32 MHz bandwidth and 128 channels. The second frequency of each pair was configured for continuum observations with 128 MHz bandwidth each. The system temperatures were typically 60 K. The (naturally-weighted) synthesized half-power beam width was $2.8'' \times 1.9''$ with P.A. 72° for H 214, $3.9'' \times 1.9''$ with P.A. -86° for H 168, and $6.9'' \times 5.4''$ with P.A. -73° for H 75. The combination of H 214 and H 168 yields a synthesized half-power beam width of $3.0'' \times 1.9''$ with P.A.

82°, and the combination of all three configurations a synthesized half-power beam width of $3.4'' \times 2.3''$ with P.A. 83°. The primary beam was $\sim 2.4'$ FWHM. The correlator bandpass was calibrated on PKS 1253–055. The phase and gain calibration was determined on the nearby source PKS 1759–39. The absolute flux density scale was derived from Uranus. The absolute calibration uncertainty is estimated to be $\sim 20\%$. The data were calibrated, continuum subtracted, imaged, and deconvolved using the software package MIRIAD (Sault et al. 1995).

Our ATCA data are affected by two problems. First, the tuning frequency used in May was not updated for the new observatory velocity in July and September. As a result, the observed bands were shifted by +12 and +16 MHz in rest frequency in the H 168 and H 75 configurations with respect to the H 214 configuration. Second, we suspect a technical problem with the tuning at 99 GHz in May and July because we do not detect any line in the H 214 and H 168 configurations while we easily detect two lines in the H 75 configuration: one unidentified line and one line from $\text{CH}_3\text{CH}_2\text{CO}$, $v_t=1$ according to our line survey with the IRAM 30m telescope. Comparing this band to the two other bands where we detect every line in each configuration (albeit with different intensities due to variable spatial filtering), we consider it to be very unlikely that the two lines detected at 99 GHz in the H 75 configuration are completely filtered out in the H 214 and H 168 configurations. Since the amino acetonitrile transition is shifted out of the H 75 band at 99 GHz (due to the variation of the observatory velocity), we do not analyze this dataset in the present article.

2.4. Interferometric observations with the VLA

We used the NRAO Very Large Array to search for the $1_{01} - 0_{00}$ multiplet of amino acetonitrile at 9071.208 MHz and examine the possibility of cold extended emission from this molecule. The VLA data were taken over a 1.5 h interval on February 13th, 2003 when the array was in its lowest-resolution (D) configuration. Three ~ 20 minute long scans of the following position in Sgr B2 were alternated with scans of the phase calibrator NRAO 530. For absolute flux density calibration, 3C286 was observed. Our phase center in Sgr B2 was at $\alpha_{J2000}=17^{\text{h}}47^{\text{m}}20^{\text{s}}.00$, $\delta_{J2000}=-28^{\circ}22'51.0''$. This is 32'' South and 14'' North of our 30m telescope pointing positions for Sgr B2(N) and (M), respectively.

Our observations were done in spectral line mode with one intermediate frequency (IF) band split into 32 channels, each of which had a width of 0.1953 MHz, corresponding to 6.46 km s⁻¹. The usable central 72% frequency range of the IF bandwidth, 4.49 MHz, covered all the multiplet's 7 hyperfine structure (hfs) components¹. This frequency range corresponds to a total velocity coverage of 148 km s⁻¹. The center velocity was set to $V_{\text{lsr}} = 65$ km s⁻¹. A 4.49 MHz bandwidth "pseudo continuum" database (the so-called "channel 0") was created by averaging the central 23 channels. The uv -data were calibrated using the NRAO's Astronomical Imaging Processing System (AIPS). Several iterations of self calibration delivered a high quality continuum image. Using UVLIN, the average of selected regions of the line uv -database were subtracted chan-

¹ The $1_{01} - 0_{00}$ multiplet consists of 9 hyperfine components with significant intensity spanning the frequency range from 9070.233 to 9073.867 MHz. Twice two components have basically the same frequency (difference of about 0.1 kHz) so that under favorable conditions there are 7 hyperfine lines observable. Full spectroscopic information for amino acetonitrile can be found in the CDMS (entry 56507).

Table 1. Spectroscopic parameters^a (MHz) of amino acetonitrile.

Parameter	Value
A	30 246.456 1 (71)
B	4 761.061 02 (84)
C	4 310.751 23 (76)
$D_K \times 10^3$	676.62 (99)
$D_{JK} \times 10^3$	-55.298 6 (69)
$D_J \times 10^3$	3.068 53 (68)
$d_1 \times 10^6$	-671.60 (40)
$d_2 \times 10^6$	-28.893 (106)
$H_K \times 10^6$	30. ^b
$H_{KJ} \times 10^6$	-2.686 1 (268)
$H_{JK} \times 10^9$	-120.1 (72)
$H_J \times 10^9$	9.593 (276)
$h_1 \times 10^9$	2.989 (225)

(a) Watson's S -reduction was employed in the representation I' . The dimensionless weighted rms of the fit is 0.51, therefore, the numbers in parentheses may be considered as two standard deviations in units of the least significant figures.

(b) Assumed value (see Sect. 3.1).

nel by channel from the latter to remove the continuum level. To calibrate the spectral line data, the phase and amplitude corrections determined by the initial calibration, as well as by the self calibration were transferred to the line database and applied to them successively, producing a 23 channel database which was imaged channel by channel using natural weighting. The synthesized beam width of the images is $20.5'' \times 7.0''$ FWHM with a position angle of -6.3° East of North².

3. Identification of amino acetonitrile

3.1. Amino acetonitrile frequencies

In the course of the present investigation an amino acetonitrile entry (tag: 56507) has been prepared for the catalog of the Cologne Database for Molecular Spectroscopy (CDMS, see Müller et al. 2001, 2005). The laboratory transition frequencies were summarized by Bogey, Dubus, & Guillemin (1990). Their work included microwave transitions reported without ¹⁴N quadrupole splitting by MacDonald & Tyler (1972), Pickett (1973), as well as microwave transitions reported with quadrupole splitting by Brown et al. (1977); the latter data were used with the reported splitting. Line fitting and prediction of transition frequencies was done with the SPFIT/SPCAT suite of programs (Pickett 1991) using a Watson type Hamiltonian in the S reduction in the representation I' (see, e.g., Gordy & Cook 1984).

The set of spectroscopic parameters reported by Bogey et al. (1990) included terms of up to decic order (S_K), rather unusual for an apparently rigid and fairly heavy molecule, and we found the higher order parameters to be surprisingly large. Moreover, the off-diagonal sextic distortion parameter h_3 was larger in magnitude than h_2 , and h_1 was not even used in the fit; the importance of these parameters is reversed to what is more commonly found. Therefore, we performed a trial fit with the octic and decic parameters as well as h_2 and h_3 omitted and the sextic term

² The calibrated and deconvolved data cubes and images (line and continuum) obtained with the PdBI, the ATCA, and the VLA are available in FITS format at the CDS via anonymous ftp to cdsarc.u-strasbg.fr (130.79.128.5) or via <http://cdsweb.u-strasbg.fr/cgi-bin/qcat?J/A+A/>.

H_K fixed to a value that was estimated from $A/D_K \approx D_K/H_K$. Subsequently, we found that inclusion of h_1 improved the quality of the fit. All transitions but five having $\Delta K_a \geq 1$ and $K_a'' \geq 3$ could be reproduced well. Two of these had $K_a = 3 - 2$ and deviated ~ 3.5 MHz from the predicted frequencies which was only twice the predicted uncertainty. The inclusion of these transitions in the fit caused relatively small changes in A and D_K ; changes in the remaining parameters were within the uncertainties. Therefore, it is likely that the assignments of these two transitions are correct. Effects on the predicted $\Delta K_a = 0$ transition frequencies are negligible. The remaining three transitions are considered to be misassignments as their inclusion would require many more higher order distortion parameters with apparently unphysical values and a poorer quality of the fit. Hence, those transitions were omitted from our fit. The resulting spectroscopic parameters are given in Table 1. The rotational partition function at 75 and 150 K is 4403 and 12460, respectively.

3.2. Modeling of the 30m line survey

The average line density above 3σ in our 30m survey is about 100 and 25 features per GHz for Sgr B2(N) and (M), respectively, translating into about 3700 and 950 lines over the whole 80–116 GHz band. To identify a new molecule in such a line forest and reduce the risk of mis-assignments, it is essential to model first the emission of all known molecules, including vibrationally and torsionally excited states, and their isotopologues. We used the XCLASS software (see Comito et al. 2005 and references therein) to model the emission and absorption lines in the LTE approximation. These calculations take into account the beam dilution, the line opacity, and the line blending. The molecular spectroscopic parameters are taken from our line catalog which contains all entries from the CDMS catalog (Müller et al. 2001, 2005) and from the molecular spectroscopic database of the Jet Propulsion Laboratory (JPL, see Pickett et al. 1998), plus additional “private” entries.

Each molecule is modeled separately with the following set of input parameters: source size, rotational temperature, column density, velocity linewidth, velocity offset with respect to the systemic velocity of the source, and a flag indicating if it is an emission or absorption component. For some of the molecules, it was necessary to include several velocity components to reproduce the observed spectra. The velocity components in emission are supposed to be non-interacting, i.e. the intensities add up linearly. The radiative transfer is computed in the following way: first the emission line spectrum is calculated, and then the absorption lines, using the full (lines + continuum) emission spectrum as background to absorb against. The vibrationally and/or torsionally excited states of some molecules were modeled separately from the ground state. The input parameters were varied until a good fit to the data was obtained for each molecule. The whole spectrum including all the identified molecules was then computed at once, and the parameters for each molecule were adjusted again when necessary. The quality of the fit was checked by eye over the whole frequency coverage of the line survey. We favored our eye-checking method against an automated fitting because the high occurrence of line blending and the uncertainty in the baseline removal would in many cases make an automated fitting procedure fail.

The detailed results of this modeling will be published in a forthcoming article describing the complete survey (Belloche et al., *in prep*). So far, we have identified 51 different molecules, 60 isotopologues, and 41 vibrationally/torsionally excited states in Sgr B2(N), which represent about 60% of the lines detected

Table 4. Parameters of our best-fit LTE model of amino acetonitrile.

Size ^a	T _{rot}	N _{AAN} ^b	FWHM	V _{off} ^c
(")	(K)	(cm ⁻²)	(km s ⁻¹)	(km s ⁻¹)
(1)	(2)	(3)	(4)	(5)
2.0	100	2.80×10^{16}	7.0	0.0

(a) Source diameter (FWHM).

(b) Column density of amino acetonitrile.

(c) Velocity offset with respect to the systemic velocity of Sgr B2(N) $V_{\text{lsr}} = 64 \text{ km s}^{-1}$.

above the 3σ level. In Sgr B2(M), the corresponding numbers are 41, 50, 20, and 50%, respectively.

3.3. Detection of amino acetonitrile with the 30m telescope

We consider it essential for claiming a detection of a new molecule that all lines of this molecule in our observed bands are consistent with this claim, i.e. are either detected or blended with lines of other species. Therefore, in the following, we inspect all transitions of amino acetonitrile in our frequency range. Our line survey at 3, 2, and 1.3 mm covers 596 transitions of our amino acetonitrile catalog ($v=0$ only). Our LTE modeling shows, however, that the transitions with the line strength times the appropriate (a - or b -type) dipole moment squared, $S\mu^2$, smaller than 20 D^2 are much too weak to be detectable with the sensitivity we achieved. Therefore, we list in Table 2 (*online material*) only the 398 transitions above this threshold. To save some space, when two transitions have a frequency difference smaller than 0.1 MHz which cannot be resolved, we list only the first one. We number the transitions in Col. 1 and give their quantum numbers in Col. 2. The frequencies, the frequency uncertainties, the energies of the lower levels in temperature units, and the $S\mu^2$ values are listed in Col. 3, 4, 5, and 6, respectively. Since the spectra are in most cases close to the line confusion limit and it is difficult to measure the noise level, we give in Col. 7 the rms sensitivity computed from the system temperature and the integration time: $\sigma = \frac{F_{\text{eff}}}{B_{\text{eff}}} \times \frac{2T_{\text{sys}}}{\sqrt{\delta f t}}$, with F_{eff} and B_{eff} the forward and beam efficiencies, T_{sys} the system temperature, δf the spectral resolution, and t the total integration time (on-source plus off-source).

We list in Col. 8 of Table 2 comments about the blends affecting the amino acetonitrile transitions. As can be seen in this table, most of the amino acetonitrile lines covered by our survey of Sgr B2(N) are heavily blended with lines of other molecules and therefore cannot be identified in this source. Only 88 of the 398 transitions are relatively free of contamination from other molecules, known or still unidentified according to our modeling. They are marked “Detected” or “Group detected” in Col. 8 of Table 2, and are listed with more information in Table 3. They correspond to 51 observed features which are shown in Fig. 1 (*online material*) and labeled in Col. 8 of Table 3. For reference, we show the spectrum observed toward Sgr B2(M) in this figure also. We identified the amino acetonitrile lines and the blends affecting them with the LTE model of this molecule and the LTE model including all molecules (see Sect. 3.2). The parameters of our best-fit LTE model of amino acetonitrile are listed in Table 4, and the model is overlaid in red on the spectrum observed toward Sgr B2(N) in Fig. 1. The best-fit LTE model including all molecules is shown in green in the same figure. The source size

Table 3. Transitions of amino acetonitrile detected toward Sgr B2(N) with the IRAM 30m telescope.

N^a	Transition	Frequency (MHz)	Unc. ^b (kHz)	E_l^c (K)	$S\mu^2$ (D ²)	σ^d (mK)	F^e	τ^f	I_{obs}^g (K km/s)	I_{AAN}^g (K km/s)	I_{all}^g (K km/s)	Comments
(1)	(2)	(3)	(4)	(5)	(6)	(7)	(8)	(9)	(10)	(11)	(12)	(13)
1	9 _{0,9} - 8 _{0,8}	80947.479	7	16	60	33	1	0.13	0.65(16)	0.38	0.42	no blend
3	9 _{5,5} - 8 _{5,4}	81700.966	6	47	41	13	2	0.16	0.92(07)	0.67	0.75	partial blend with U-line
4	9 _{5,4} - 8 _{5,3}	81700.967	6	47	41	13	2	-	-	-	-	-
5	9 _{6,3} - 8 _{6,2}	81702.498	5	60	33	13	2	-	-	-	-	-
6	9 _{6,4} - 8 _{6,3}	81702.498	5	60	33	13	2	-	-	-	-	-
7	9 _{4,6} - 8 _{4,5}	81709.838	6	35	48	13	3	0.23	0.39(06)	0.66	0.73	no blend
8	9 _{7,2} - 8 _{7,1}	81709.848	6	76	24	13	3	-	-	-	-	-
9	9 _{7,3} - 8 _{7,2}	81709.848	6	76	24	13	3	-	-	-	-	-
10	9 _{4,5} - 8 _{4,4}	81710.098	6	35	48	13	3	-	-	-	-	-
11	9 _{3,7} - 8 _{3,6}	81733.892	6	27	53	13	4	0.11	0.50(06)	0.32	1.46	blend with CH ₃ OCH ₃ and HCC ¹³ CN, $v_6=1$
12	9 _{3,6} - 8 _{3,5}	81756.174	6	27	53	13	5	0.11	0.39(06)	0.32	0.32	blend with U-line
13	9 _{2,7} - 8 _{2,6}	82224.644	7	21	57	19	6	0.12	0.19(08)	0.36	0.35	uncertain baseline
17	10 _{2,9} - 9 _{2,8}	90561.332	6	25	64	20	7	0.14	0.64(09)	0.52	1.01	blend with weak C ₂ H ₅ CN, $v_{13}=1/v_{21}=1$
18	10 _{6,4} - 9 _{6,3}	90783.538	6	64	43	14	8	0.28	1.54(06)	1.05	1.40	partial blend with CH ₂ (OH)CHO and U-line
19	10 _{6,5} - 9 _{6,4}	90783.538	6	64	43	14	8	-	-	-	-	-
20	10 _{5,6} - 9 _{5,5}	90784.281	6	50	50	14	8	-	-	-	-	-
21	10 _{5,5} - 9 _{5,4}	90784.285	6	50	50	14	8	-	-	-	-	-
22	10 _{7,3} - 9 _{7,2}	90790.259	6	80	34	14	9	0.09	0.51(06)	0.33	0.56	blend with U-line
23	10 _{7,4} - 9 _{7,3}	90790.259	6	80	34	14	9	-	-	-	-	-
24	10 _{4,7} - 9 _{4,6}	90798.685	6	39	56	14	10	0.21	1.42(06)	0.81	0.95	blend with U-line
25	10 _{4,6} - 9 _{4,5}	90799.249	6	39	56	14	10	-	-	-	-	-
28	10 _{3,8} - 9 _{3,7}	90829.945	6	31	60	14	11	0.13	0.84(06)	0.47	0.51	blend with U-line also in M?
29	10 _{3,7} - 9 _{3,6}	90868.038	6	31	60	14	12	0.13	0.49(06)	0.47	0.57	partial blend with U-line
30	10 _{2,8} - 9 _{2,7}	91496.108	8	25	64	24	13	0.15	0.86(11)	0.53	0.71	partial blend with CH ₃ CN, $v_4=1$ and U-line
32	11 _{1,11} - 10 _{1,10}	97015.224	8	25	72	21	14	0.18	2.05(09)	0.71	1.78	partial blend with C ₂ H ₅ OH and CH ₃ OCHO
47	11 _{3,9} - 10 _{3,8}	99928.886	6	35	68	14	15	0.15	1.31(06)	0.66	1.24	partial blend with NH ₂ CN and U-line
48	11 _{3,8} - 10 _{3,7}	99990.567	7	35	68	14	16	0.15	0.80(06)	0.66	0.74	no blend
49	11 _{2,9} - 10 _{2,8}	100800.876	8	29	71	20	17	0.17	1.38(08)	0.75	1.25	partial blend with CH ₃ CH ₃ CO, $v=0$ and U-line
50	11 _{1,10} - 10 _{1,9}	101899.795	8	26	72	34	18	0.18	0.56(14)	0.81	0.88	uncertain baseline
51	12 _{1,12} - 11 _{1,11}	105777.991	8	29	79	43	19	0.20	1.98(18)	0.95	2.88	blend with c-C ₂ H ₄ O and C ₂ H ₅ CN, $v=0$
52	12 _{0,12} - 11 _{0,11}	107283.142	8	29	80	24	20	0.21	2.67(10)	1.00	2.01	blend with C ₂ H ₅ OH and U-line
53	12 _{2,11} - 11 _{2,10}	108581.408	7	34	77	20	21	0.19	1.49(08)	0.97	1.94	weak blend with C ₂ H ₅ OH
58	12 _{5,8} - 11 _{5,7}	108956.206	6	60	66	29	22	0.26	2.19(11)	1.34	3.44	blend with C ₂ H ₅ OH
59	12 _{5,7} - 11 _{5,6}	108956.229	6	60	66	29	22	-	-	-	-	-
68	12 _{3,10} - 11 _{3,9}	109030.225	6	40	75	29	23	0.18	1.67(11)	0.89	1.24	partial blend with HC ₃ N, $v_4=1$, C ₂ H ₅ OH, and U-line
71	12 _{1,11} - 11 _{1,10}	111076.901	8	31	79	25	24	0.21	1.16(10)	1.08	1.39	slightly shifted?
72	13 _{1,13} - 12 _{1,12}	114528.654	8	34	86	37	25	0.23	2.49(15)	1.23	1.42	partial blend with U-line
84	15 _{10,5} - 14 _{10,4}	136248.969	10	169	55	28	26	0.09	2.10(10)	0.72	1.03	blend with U-line
85	15 _{10,6} - 14 _{10,5}	136248.969	10	169	55	28	26	-	-	-	-	-
89	15 _{4,11} - 14 _{4,10}	136303.599	6	65	93	28	27	0.21	3.99(09)	1.62	4.02	blend with a(CH ₂ OH) ₂ and CH ₃ C ₃ N
92	15 _{3,13} - 14 _{3,12}	136341.155	6	57	96	28	28	0.24	2.92(10)	1.81	2.22	partial blend with U-line also in M
103	16 _{5,12} - 15 _{5,11}	145325.871	30	83	96	25	29	0.39	2.89(08)	3.30	4.80	uncertain baseline, partial blend with C ₂ H ₅ CN, $v_{13}=1/v_{21}=1$
104	16 _{5,11} - 15 _{5,10}	145326.209	30	83	96	25	29	-	-	-	-	-

Notes: (a) Numbering of the observed transitions with $S\mu^2 > 20 \text{ D}^2$ (see Table 2). (b) Frequency uncertainty. (c) Lower energy level in temperature units (E_l/k_B). (d) Calculated rms noise level in T_{mb} scale. (e) Numbering of the observed features. (f) Peak opacity of the amino acetonitrile modeled feature. (g) Integrated intensity in T_{mb} scale for the observed spectrum (col. 10), the amino acetonitrile model (col. 11), and the model including all molecules (col. 12). The uncertainty in col. 10 is given in parentheses in units of the last digit.

we used to model the amino acetonitrile emission was derived from our interferometric measurements (see Sect. 3.4 below).

For the frequency range corresponding to each observed amino acetonitrile feature, we list in Table 3 the integrated intensities of the observed spectrum (Col. 10), of the best-fit model of amino acetonitrile (Col. 11), and of the best-fit model including

all molecules (Col. 12). In these columns, the dash symbol indicates transitions belonging to the same feature. Columns 1 to 7 are the same as in Table 2. The 1σ uncertainty given in Col. 10 was computed using the estimated noise level of Col. 7. These measurements are plotted in the form of a population diagram in Fig. 2, which plots upper level column density divided by statis-

Table 3. (continued)

N^a	Transition	Frequency (MHz)	Unc. ^b (kHz)	E_l^c (K)	$S\mu^2$ (D ²)	σ^d (mK)	F^e	τ^f	I_{obs}^g (K km/s)	I_{AAN}^g (K km/s)	I_{all}^g (K km/s)	Comments
(1)	(2)	(3)	(4)	(5)	(6)	(7)	(8)	(9)	(10)	(11)	(12)	(13)
105	16 _{10,6} - 15 _{10,5}	145330.985	40	175	65	25	30	0.11	0.97(07)	0.92	1.02	uncertain baseline
106	16 _{10,7} - 15 _{10,6}	145330.985	40	175	65	25	30	-	-	-	-	-
115	16 _{3,14} - 15 _{3,13}	145443.850	30	63	103	25	31	0.25	4.33(08)	2.18	4.68	blend with C ₂ H ₅ CN, v=0 and U-line
118	16 _{1,15} - 15 _{1,14}	147495.789	6	55	106	31	32	0.29	3.27(11)	2.54	11.47	partial blend with H ₃ C ¹³ CN, v ₈ =1
139	17 _{4,13} - 16 _{4,12}	154542.406	5	79	107	112	33	0.44	13.25(42)	4.63	5.52	blend with U-line
140	17 _{3,15} - 16 _{3,14}	154544.046	5	70	109	112	33	-	-	-	-	-
145	18 _{7,12} - 17 _{7,11}	163454.794	5	127	101	38	34	0.49	10.38(13)	5.32	16.48	partial blend with HC ¹³ CCN, v ₆ =1 and HCC ¹³ CN, v ₆ =1
146	18 _{7,11} - 17 _{7,10}	163454.794	5	127	101	38	34	-	-	-	-	-
147	18 _{8,10} - 17 _{8,9}	163456.136	6	146	96	38	34	-	-	-	-	-
148	18 _{8,11} - 17 _{8,10}	163456.136	6	146	96	38	34	-	-	-	-	-
149	18 _{9,9} - 17 _{9,8}	163470.472	8	166	90	38	35	0.41	15.17(14)	5.57	21.97	partial blend with HCC ¹³ CN, v ₇ =1
150	18 _{9,10} - 17 _{9,9}	163470.472	8	166	90	38	35	-	-	-	-	-
151	18 _{6,13} - 17 _{6,12}	163473.305	5	111	106	38	35	-	-	-	-	-
152	18 _{6,12} - 17 _{6,11}	163473.321	5	111	106	38	35	-	-	-	-	-
155	18 _{11,7} - 17 _{11,6}	163525.533	11	216	75	38	36	0.49	10.26(13)	5.27	17.96	blend with HC ₃ N, v ₄ =1
156	18 _{11,8} - 17 _{11,7}	163525.533	11	216	75	38	36	-	-	-	-	-
157	18 _{5,14} - 17 _{5,13}	163526.183	4	97	110	38	36	-	-	-	-	-
158	18 _{5,13} - 17 _{5,12}	163527.171	4	97	110	38	36	-	-	-	-	-
163	18 _{4,15} - 17 _{4,14}	163635.326	5	86	114	38	37	0.25	4.08(11)	2.82	5.01	partial blend with C ₃ H ₇ CN
164	18 _{3,16} - 17 _{3,15}	163640.468	5	78	116	38	38	0.28	4.65(11)	2.99	6.77	partial blend with C ₃ H ₇ CN
177	19 _{6,14} - 18 _{6,13}	172566.092	50	119	114	44	39	0.38	10.01(14)	4.39	6.43	partial blend with U-line and HCC ¹³ CN, v ₇ =1
178	19 _{6,13} - 18 _{6,12}	172566.092	50	119	114	44	39	-	-	-	-	-
227	23 _{4,20} - 22 _{4,19}	209272.189	6	130	148	58	40	0.26	7.29(29)	4.62	14.85	blend CH ₃ CH ₃ CO, v=0
237	23 _{1,22} - 22 _{1,21}	209629.913	9	113	152	45	41	0.32	9.03(24)	5.54	30.88	blend with HC ¹³ CCN, v ₇ =2 and HCC ¹³ CN, v ₇ =2
247	25 _{9,16} - 24 _{9,15}	227040.487	50	230	145	96	42	0.29	9.58(55)	9.45	35.33	partial blend with CN absorption and CH ₃ CH ₃ CO, v ₁ =1
248	25 _{9,17} - 24 _{9,16}	227040.487	50	230	145	96	42	-	-	-	-	-
249	25 _{8,18} - 24 _{8,17}	227045.287	50	210	149	96	42	-	-	-	-	-
250	25 _{8,17} - 24 _{8,16}	227045.287	50	210	149	96	42	-	-	-	-	-
251	25 _{10,15} - 24 _{10,14}	227055.944	50	254	139	96	43	0.15	-0.64(44)	3.29	3.62	partial blend with CN absorption
252	25 _{10,16} - 24 _{10,15}	227055.944	50	254	139	96	43	-	-	-	-	-
253	25 _{7,19} - 24 _{7,18}	227079.847	50	191	153	96	44	0.32	10.94(44)	7.16	57.69	blend with CH ₂ CH ¹³ CN and CH ₃ OH, v=0
254	25 _{7,18} - 24 _{7,17}	227079.847	50	191	153	96	44	-	-	-	-	-
273	25 _{2,23} - 24 _{2,22}	231485.527	50	138	165	40	45	0.30	12.73(19)	6.27	6.60	blend with U-line?
292	26 _{6,21} - 25 _{6,20}	236269.491	60	186	163	37	46	0.36	15.53(18)	8.02	14.17	partial blend with t-C ₂ H ₅ OCHO and U-line
293	26 _{6,20} - 25 _{6,19}	236270.459	60	186	163	37	46	-	-	-	-	-
306	28 _{0,28} - 27 _{0,27}	244765.968	21	160	186	39	47	0.28	9.56(19)	6.62	10.35	blend with CH ₃ ¹³ CH ₂ CN, v=0 and U-line
322	27 _{6,22} - 26 _{6,21}	245378.722	10	197	170	72	48	0.35	16.69(36)	8.29	22.21	blend with ¹³ CH ₃ CH ₂ CN, v=0?
323	27 _{6,21} - 26 _{6,20}	245380.146	10	197	170	72	48	-	-	-	-	-
368	29 _{9,20} - 28 _{9,19}	263364.923	22	277	174	74	49	0.26	6.72(37)	8.51	9.17	baseline problem?, blend with U-line
369	29 _{9,21} - 28 _{9,20}	263364.923	22	277	174	74	49	-	-	-	-	-
370	29 _{10,19} - 28 _{10,18}	263368.355	26	300	170	74	49	-	-	-	-	-
371	29 _{10,20} - 28 _{10,19}	263368.355	26	300	170	74	49	-	-	-	-	-
384	29 _{6,24} - 28 _{6,23}	263604.573	12	221	184	74	50	0.28	10.29(36)	8.81	14.22	baseline problem?, partial blend with CH ₃ CH ₃ CO, v ₁ =1 and CH ₃ OCH ₃
385	29 _{6,23} - 28 _{6,22}	263607.689	12	221	184	74	50	-	-	-	-	-
398	29 _{4,26} - 28 _{4,25}	264055.836	13	197	189	108	51	0.22	18.36(49)	5.92	14.22	partial blend with C ₂ H ₅ CN, v=0 and CH ₃ CH ₃ CO, v=0

tical weight, N_u/g_u , versus the upper level energy in Kelvins (see Goldsmith & Langer 1999). The data are shown in black and our best-fit model of amino acetonitrile in red. Out of 21 features encompassing several transitions, 10 contain transitions with different energy levels and were ignored in the population diagram

(features 2, 3, 8, 33, 34, 35, 36, 42, and 49). We used equation A5 of Snyder et al. (2005) to compute the ordinate values. This equation assumes optically thin emission. To estimate by how much line opacities affect this diagram, we applied the opacity correction factor $C_\tau = \frac{\tau}{1-e^{-\tau}}$ (see Goldsmith & Langer 1999;

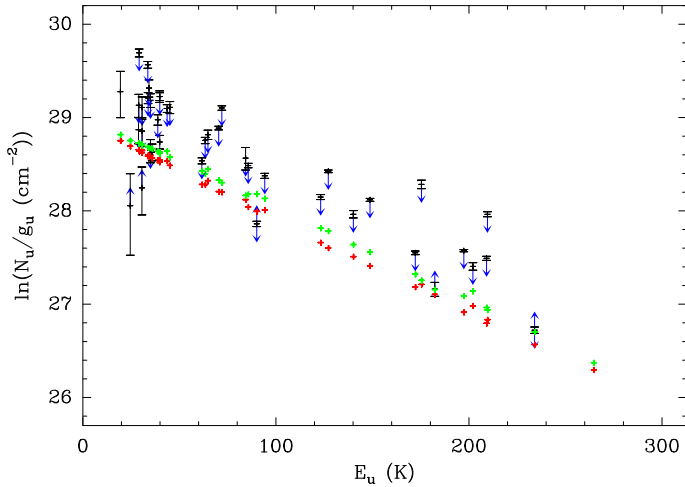


Fig. 2. Population diagram of amino acetonitrile in Sgr B2(N). The red points were computed in the optically thin approximation using the integrated intensities of our best-fit *model* of amino acetonitrile, while the green points were corrected for the opacity. The black points were computed in the optically thin approximation using the integrated intensities of the spectrum *observed* with the IRAM 30m telescope. The error bars are 1σ uncertainties on N_u/g_u . Blue arrows pointing downwards mark the transitions blended with transitions from other molecules, while blue arrows pointing upwards indicate that the baseline removed in the observed spectrum is uncertain. The arrow length is arbitrary. The measurement corresponding to feature 43 (at $E_u/k_B = 265$ K) is not shown since the integrated intensity measured toward Sgr B2(N) is negative, due to the blend with CN absorption lines.

Snyder et al. 2005) to the modeled intensities, using the opacities from our radiative transfer calculations (Col. 9 of Table 3); the result is shown in green in Fig. 2. The population diagram derived from the modeled spectrum is slightly shifted upwards but its shape, in particular its slope (the inverse of which *approximately* determines the rotation temperature), is not significantly changed, since $\ln C_T$ does not vary much (from 0.04 to 0.24). The populations derived from the *observed* spectrum in the optically thin approximation are therefore not significantly affected by the optical depth of the amino acetonitrile transitions³. The scatter of the black crosses in Fig. 2 is therefore dominated by the blends with other molecules and uncertainties in the baseline removal (indicated by the downwards and upwards blue arrows, respectively). From this analysis, we conclude that our best-fit model for amino acetonitrile is fully consistent with our 30m data of Sgr B2(N).

Finally, as mentioned above, the 310 transitions of Table 2 not shown in Fig. 1 are all but one heavily blended with transitions of other molecules and cannot be clearly identified in Sgr B2(N). The single exception is amino acetonitrile transition 192 shown in Fig. 3. There are too many blended lines in this frequency range to properly remove the baseline. It is very uncertain and the true baseline is most likely at a lower level than computed here. The presence of several H^{13}CN 2–1 velocity components in absorption also complicates the analysis. Therefore it is very likely that the (single) apparent disagreement concerning transition 192 between our best-fit model and

³ Note that our modeled spectrum is anyway calculated with the full LTE radiative transfer which takes into account the optical depth effects (see Sect. 3.2).

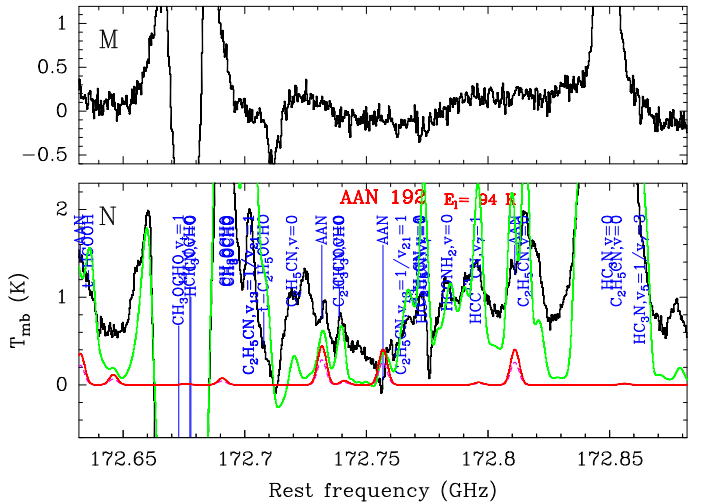


Fig. 3. Spectrum obtained toward Sgr B2(N) (bottom) and Sgr B2(M) (top) with the IRAM 30m telescope at the frequency of amino acetonitrile (AAN) transition 192 (see caption of Fig. 1 for more details about the color coding). There are too many blended lines in the spectrum of Sgr B2(N) to properly remove the baseline, which is very uncertain and most likely at a lower level than could be computed here. This is the only discrepancy concerning the amino acetonitrile lines in the whole survey. The absorption lines, particularly strong in the spectrum of Sgr B2(M), are velocity components of H^{13}CN 2–1.

the 30m spectrum observed toward Sgr B2(N) is not real and does not invalidate our claim of detection of amino acetonitrile.

3.4. Mapping amino acetonitrile with the PdBI

The two 3 mm spectral windows of the PdBI were chosen to cover the five amino acetonitrile features F2 to F6. The spectra toward Sgr B2(N) are shown for both windows toward 3 positions P1, P2, and P3 in Fig. 4a to f. Many lines are detected, the strongest one being a line from within the vibrationally excited state $v_7=1$ of cyanoacetylene (HC_3N) at 82.2 GHz. We also easily detect lines from within its vibrationally excited state $v_4=1$, from its isotopologues HC^{13}CCN and HCC^{13}CN in the $v_7=1$ state, from ethyl cyanide ($\text{C}_2\text{H}_5\text{CN}$), as well as two unidentified lines at 82.213 and 82.262 GHz. At a lower level, we find emission for all the amino acetonitrile features F2 to F6, and we also detect methylformate (CH_3OCHO).

The integrated intensity maps of the amino acetonitrile features F2 to F6 are presented in Fig. 5a to e, along with two maps of ethyl cyanide (Fig. 5g and h), four maps of cyanoacetylene in the vibrationally excited states $v_4=1$ and $v_7=1$ (Fig. 5j to m), one map of its isotopologue HC^{13}CCN in the state $v_7=1$ (Fig. 5i), one map of methylformate (Fig. 5n), and a reference map computed on the PdBI line-free frequency range between F2 and F3 (Fig. 5f). The frequency intervals used to compute the integrated intensities are given in Col. 3 and 4 of Table 5 and shown with dotted lines in Fig. 4. We used the fitting routine GAUSS_2D of the GILDAS software to measure the position, size, and peak flux of each integrated emission. The results are listed in Col. 6 to 11 in Table 5. We label P1 the mean peak position of features F2 to F6, P2 the northern peak position of ethyl cyanide, and P3 the peak position of methylformate (see Table 6 and the plus symbols in Fig. 5). Finally, the PdBI velocity-integrated flux spa-

Table 5. Measurements obtained toward Sgr B2(N) with the IRAM Plateau de Bure interferometer at 82 GHz.

Molecule	F ^a	f _{min} ^b	f _{max} ^b	σ ^c	F _{peak} ^d	Δα ^d	Δδ ^d	θ _{maj} ^d	θ _{min} ^d	P.A. ^d	Φ _{PdBI} ^e	Φ _{30m} ^f
(1)	(2)	(MHz)	(MHz)	(Jy/beam km/s)	(6)	($''$)	($''$)	($''$)	($''$)	($^{\circ}$)	(Jy km/s)	(Jy km/s)
		(3)	(4)	(5)	(6)	(7)	(8)	(9)	(10)	(11)	(12)	(13)
AAN	F2	81700.21	81703.33	0.09	0.68	-1.60 ± 0.05	0.30 ± 0.22	3.9 ± 0.4	2.00 ± 0.10	20.5 ± 0.1	1.76	2.89
AAN	F3	81708.02	81712.08	0.10	0.68	-1.25 ± 0.06	0.02 ± 0.24	3.8 ± 0.5	1.39 ± 0.12	10.1 ± 0.0	1.24	1.75
AAN	F4	81732.71	81734.90	0.06	0.44	-1.70 ± 0.06	0.35 ± 0.24	3.6 ± 0.5	1.54 ± 0.12	14.0 ± 0.0	0.86	0.98
AAN	F5	81754.90	81757.40	0.06	0.24	-1.52 ± 0.10	0.03 ± 0.44	3.2 ± 0.9	1.20 ± 0.21	12.5 ± 1.1	0.30	1.15
AAN	F6	82223.46	82226.27	0.06	0.43	-1.43 ± 0.06	0.28 ± 0.24	3.5 ± 0.5	1.54 ± 0.11	6.0 ± 0.4	0.79	0.97
Reference		81704.27	81707.08	0.07
C ₂ H ₅ CN	HV	81741.77	81744.90	0.11	2.05	-1.64 ± 0.02	5.58 ± 0.09	3.8 ± 0.2	1.50 ± 0.04	5.7 ± 0.0	4.07	6.38
C ₂ H ₅ CN	LV	81745.21	81749.27	0.15	2.82	-1.74 ± 0.02	0.46 ± 0.09	3.8 ± 0.2	2.87 ± 0.04	13.7 ± 0.0	10.43	12.94
HC ¹³ CCN v ₇ =1		81726.15	81728.96	0.09	2.20	-1.35 ± 0.02	0.60 ± 0.07	3.7 ± 0.1	1.68 ± 0.03	12.6 ± 0.0	4.98	4.81
HC ₃ N v ₄ =1		81767.71	81771.15	0.10	2.14	-1.43 ± 0.02	0.28 ± 0.08	3.6 ± 0.2	1.35 ± 0.04	9.9 ± 0.0	3.78	3.85
HC ₃ N v ₇ =1 ^g	HV	82196.27	82198.77	0.25	6.17	-2.16 ± 0.02	0.69 ± 0.07	4.0 ± 0.1	1.84 ± 0.03	16.2 ± 22.5	16.05	23.88
					3.36	-1.50 ± 0.03	5.25 ± 0.12	4.0 ± 0.2	1.36 ± 0.06	5.5 ± 22.5	5.35	...
HC ₃ N v ₇ =1	LV	82199.40	82201.58	0.36	9.06	-1.67 ± 0.02	0.42 ± 0.07	3.7 ± 0.1	2.50 ± 0.03	10.2 ± 22.5	31.04	33.48
HC ₃ N v ₇ =1	RW	82202.52	82203.77	0.12	3.37	-0.71 ± 0.01	0.24 ± 0.06	3.1 ± 0.1	2.77 ± 0.03	45.0 ± 0.0	11.75	12.39
CH ₃ OCHO		82242.21	82245.33	0.10	0.67	-2.83 ± 0.06	1.23 ± 0.26	4.8 ± 0.5	2.58 ± 0.12	9.5 ± 22.5	2.83	6.62

- (a) Feature numbered like in Col. 8 of Table 3 for amino acetonitrile (AAN). HV and LV mean “high” and “low” velocity components, respectively, and RW means redshifted linewing.
- (b) Frequency range over which the intensity was integrated.
- (c) Noise level in the integrated intensity map shown in Fig. 5.
- (d) Peak flux, offsets in right ascension and declination with respect to the reference position of Fig. 5, major and minor diameters (FWHM), and position angle (East from North) derived by fitting an elliptical 2D Gaussian to the integrated intensity map shown in Fig. 5. The uncertainty in Col. 11 is the formal uncertainty given by the fitting routine GAUSS_2D, while the uncertainties correspond to the beam size divided by two times the signal-to-noise ratio in Col. 7 and 8 and by the signal-to-noise ratio in Col. 9 and 10.
- (e) Flux spatially integrated over the region showing emission in the integrated intensity map of Fig. 5.
- (f) Integrated flux of the 30m spectrum computed over the frequency range given in Col. 3 and 4.
- (g) The two emission peaks of Fig. 5k were fitted separately.

tially integrated over the emitting region is listed in Col. 12 and the 30m velocity-integrated intensity is given in Col. 13.

We present in Fig. 5o the map of continuum emission at 82.0 GHz, integrated over line-free frequency ranges. The continuum emission has a complex structure. The main region peaks at $\alpha_{J2000} = 17^{\text{h}}47^{\text{m}}19^{\text{s}}886 \pm 0^{\text{s}}005$, $\delta_{J2000} = -28^{\circ}22'18.4'' \pm 0.1''$, i.e. within $0.1''$ of the position of the ultracompact HII region K2. It also shows hints of emission at the position of the ultracompact HII regions K1 and K3, although the spatial resolution is too poor to resolve them (see, e.g., Gaume et al. 1995). There are other secondary peaks. One of them coincides with the peak of the shell-like HII region K6 while another one is located close ($< 2''$) to the peak of the shell-like HII region K5 and traces most likely the same shell. On the other hand, we detect no 3.7 mm emission at the position of the weak ultracompact HII region K9.69 (Gaume et al. 1995).

The strong lines detected with the PdBI (Fig. 5g to n) allow us to gain insight into the distribution of molecular line emission in Sgr B2(N). The double-peaked profile of ethyl cyanide seen with the 30m telescope (see Fig. 4g) is resolved with the PdBI into two sources P1 and P2 separated by about $5.3''$ (see Fig. 4a, c, Fig. 5g, h, and Table 6). P1 and P2 are spatially and kinematically coincident with the quasi-thermal methanol emission cores “i” and “h” within $0.6''$ and $0.2''$, respectively (Mehringer & Menten 1997). Cores “i” and “h” were both previously detected in ethyl cyanide (Liu & Snyder 1999; Hollis et al. 2003; Jones et al. 2007). Many molecules (but not amino acetonitrile within the limits of our sensitivity) actually show this double-peaked profile in our 30m survey of Sgr B2(N) and are most likely emitted by these two sources. P1 and P2 are also detected in our PdBI data in the vibrationally excited state $v_7=1$ of cyanoacetylene (see Fig. 4b, d, and Fig. 5k, l), and there is a hint

of emission toward P2 in the isotopologue HC¹³CCN while P1 is easily detected (see Fig. 4c and a). In addition, the wings of the main component of cyanoacetylene $v_7=1$ are spatially shifted: the redshifted wing peaks about $1''$ North-West of P1 while the blueshifted wing peaks about $1''$ East of P1 (Fig. 5m and k). This East-West velocity gradient was previously reported by several authors (e.g. Lis et al. 1993; de Vicente et al. 2000; Hollis et al. 2003). Although it could result from cloud rotation, it is most likely a sign of outflow activity (see, e.g., Liu & Snyder 1999). The transition with highest energy in our PdBI sample is a transition of cyanoacetylene in the vibrationally excited state $v_4=1$ ($E_u/k_B = 1283$ K). Within the limits of our sensitivity, we detect emission only toward P1 in this highly excited transition (Fig. 5j). Finally, methylformate peaks at a position significantly offset from P1, at $1.7''$ to the North-West (Fig. 5n). It has no counterpart in the continuum map of Fig. 5o. To sum up, our PdBI data reveal three main positions of molecular line emission (P1 and P2 corresponding to the methanol cores “i” and “h”, and P3 the peak position of methylformate), and an East-West velocity gradient around P1.

Within the limits of our sensitivity, the amino acetonitrile features F2 to F6 detected with the PdBI show only one peak, and they all peak at the same position (Fig. 5a to e). We are confident that the emission detected in features F2 to F6 is not contaminated by the continuum since no significant signal is detected in the reference map (Fig. 5f). Their weighted-mean peak position was labeled P1 above (offset $-1.5 \pm 0.2''$, $0.2 \pm 0.2''$, see Table 6). *The fact that all features are detected at the same position is consistent with their assignment to the same molecule* (see above the shifted position of methylformate for instance). The *deconvolved* major and minor axes of the emission detected in features F2 to F6 are in the range $0-2.2''$ and $1.0-1.9''$, re-

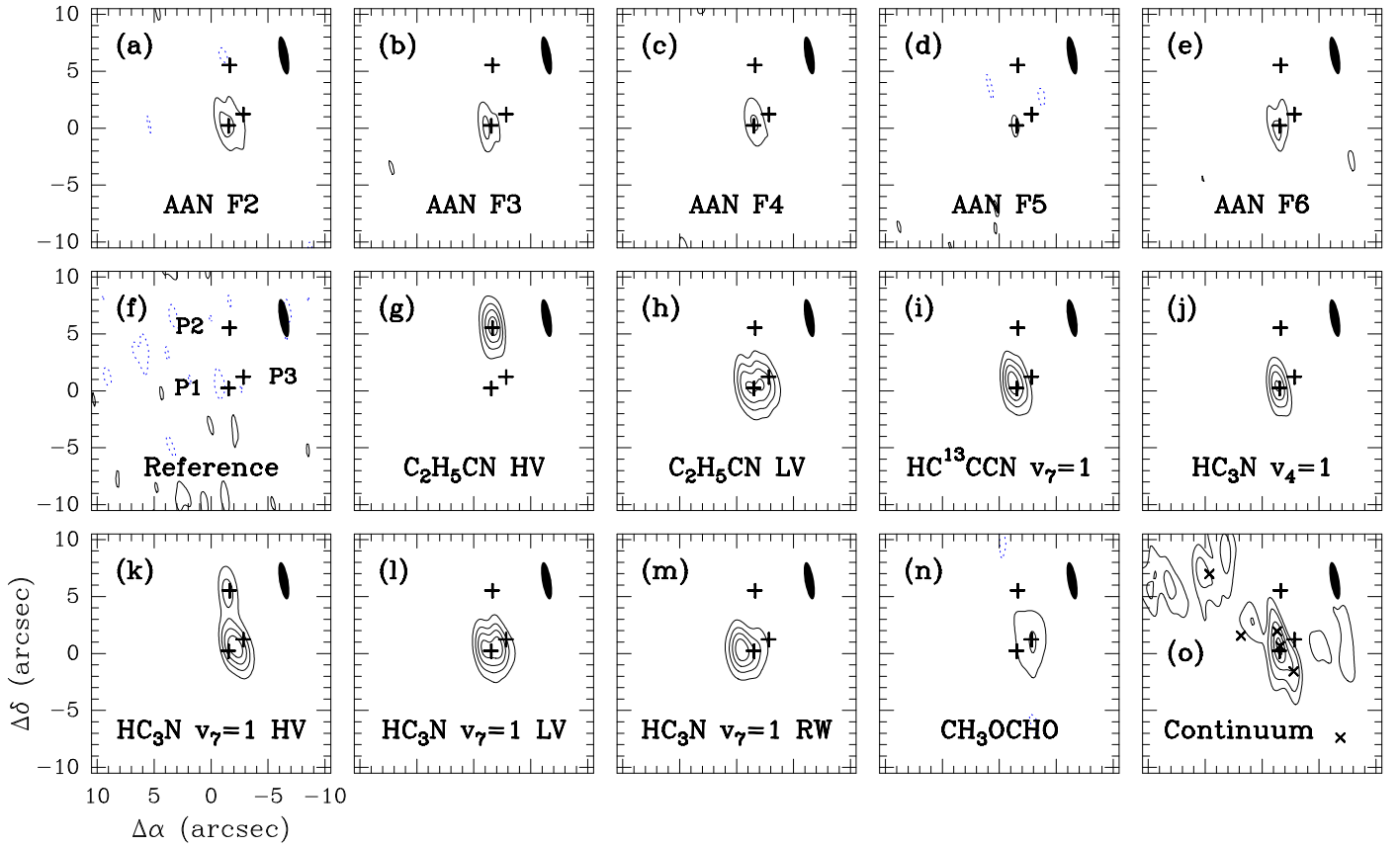


Fig. 5. Integrated intensity maps (panels **a** to **n**) and continuum map (panel **o**) obtained toward Sgr B2(N) with the Plateau de Bure interferometer at 82 GHz. Panels **a** to **e** show the amino acetonitrile (AAN) features F2 to F6 (see Fig. 4 and Table 3). Panel **f** is a reference map integrated on the emission-free frequency range between F2 and F3. Panels **g** to **n** show the other molecules listed in Table 5. The lowest contour (positive in black solid line and negative in blue dotted line) and the contour step are 2σ for panel **f**, 3σ for panels **a** to **e** and panel **n**, 4σ for panels **g** and **h**, 5σ for panels **i** to **l**, and 6σ for panel **m** (with σ given in Col. 5 of Table 5). For panel **o**, the first contours are 5σ and 10σ , and the contour step is 10σ for the other contours (with $\sigma = 8.5$ mJy/beam). In each panel, the 0,0 position is $\alpha_{J2000} = 17^{\text{h}}47^{\text{m}}20^{\text{s}}.00$, $\delta_{J2000} = -28^{\circ}22'19.0''$, the three plus symbols mark the positions P1, P2, and P3 (labeled in panel **f**), and the filled ellipse in the top right corner shows the clean beam (HPBW = $3.35'' \times 0.81''$ at P.A. = 9.7°). The cross symbols in panel **o** are the peak positions of the (ultra)compact HII regions detected by Gaume et al. (1995) at 1.3 cm (K9.69, K1, K2, K3, K5, and K6, from right to left). The spectral integration was done on the frequency ranges given in Table 5. The continuum map was computed on line-free frequency ranges. The maps are not corrected for primary beam attenuation. The amino acetonitrile features emit at the same position as the vibrationally excited state $v_4 = 1$ of cyanoacetylene. Feature F4 is partially blended with a transition from HCC^{13}CN , $v_6 = 1$.

spectively. The amino acetonitrile emission is therefore slightly resolved and has a size of roughly $2''$ FWHM, which we used for the LTE modeling. The spatially integrated fluxes of F4 and F6 agree within 20% with the fluxes measured with the 30m telescope (see Col. 12 and 13 of Table 5). The emission detected with the 30m telescope in these two features of amino acetonitrile is therefore compact ($2''$) and was not filtered out by the interferometer. The other features F2, F3, and F5 have 30m fluxes 1.6, 1.4, and 3.8 times larger than the PdBI fluxes, respectively: the emission filtered out by the interferometer most likely corresponds to the unidentified transitions blended with these amino acetonitrile features (see Fig. 4a). In addition, the low signal-to-noise ratio of feature F5 detected with the PdBI may significantly affect the flux measurement.

We used the parameters of the 30m model (see Table 4) to compute a model spectrum of amino acetonitrile with the spatial resolution of the PdBI (using the geometrical mean of the elliptical beam). The agreement with the peak spectrum is good, within a factor of 2 (see Fig. 4a and b). The small discrepancy

may come from the somewhat uncertain source size and from our approximate modeling of the interferometric beam pattern: spherical beam and full uv coverage for the model versus elliptical beam and partially sampled uv coverage for the observations. Overall, our LTE model of amino acetonitrile is therefore well consistent with the compact emission detected with the PdBI.

3.5. Mapping amino acetonitrile with the ATCA

The two 3mm spectral windows of the ATCA were chosen to cover the four amino acetonitrile features F7 to F10. The spectra toward position P4 of Sgr B2(N) (offset $-2'', 0.1''$) are presented for both windows in Fig. 6. Since the spectral windows were not exactly the same in each configuration (see Sect. 2.3), we show the spectra for each configuration (Fig. 6a to f), plus the combination of the two broadest ones (Fig. 6g and h), and the combination of all three configurations (Fig. 6i and j). Nearly all the lines seen with the 30m telescope are detected with the ATCA toward P4. In the 90.6 GHz band, we detect the blue wing of an SO_2

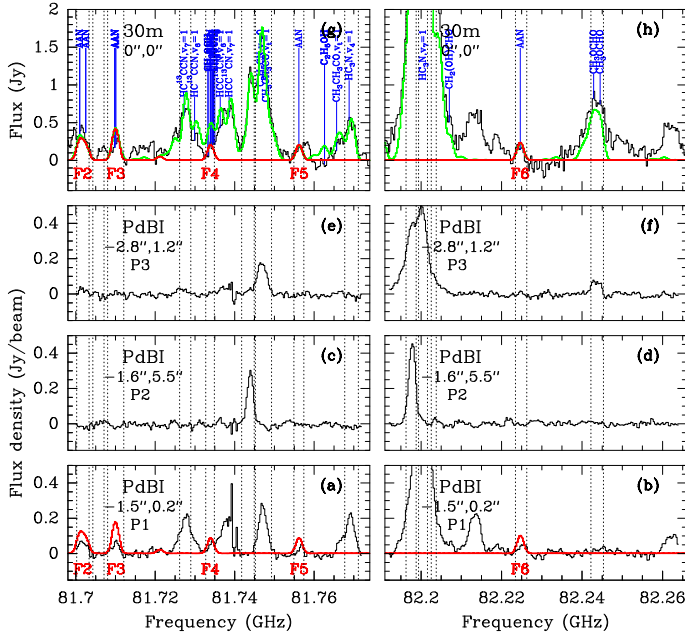


Fig. 4. Spectra obtained with the Plateau de Bure interferometer (a to f) and the 30m telescope (g and h) toward Sgr B2(N) (in black). The dotted lines show the frequency ranges listed in Table 5. The offset position with respect to the reference position of Fig. 5 is given in each panel, along with a label (P1 to P3, see their definition in Table 6). The lines identified in our 30m survey are labeled in blue. The red spectra show our best-fit model for amino acetonitrile (AAN) while the green spectrum corresponds to the 30m model including all molecules. The observed lines which have no counterpart in the green spectrum are still unidentified.

Table 6. Peak positions of continuum and molecular line emission detected with the PdBI and the ATCA toward Sgr B2(N).

	RA (J2000)	Dec (J2000)	Comments
	17 ^h 47 ^m	-28°22'	
PdBI			
82	19:886 ± 0:005	18.4" ± 0.1"	continuum 82.0 GHz
P1	19:89 ± 0:01	18.8" ± 0.2"	mean AAN ^a F2 to F6
P2	19:88 ± 0:01	13.5" ± 0.2"	mean HC ₃ N v ₇ =1, C ₂ H ₅ CN
P3	19:79 ± 0:01	17.8" ± 0.3"	peak CH ₃ OCHO
ATCA			
95	19:87 ± 0:01	18.7" ± 0.1"	mean continuum 93.2 and 97.4 GHz
P4	19:85 ± 0:02	18.9" ± 0.2"	mean AAN F7 to F10
P5	19:86 ± 0:01	13.8" ± 0.1"	mean HC ¹³ CCN v ₇ =1, CH ₃ OH v _t =1

(a) AAN stands for amino acetonitrile.

transition (Fig. 6a), the red wing of an HC¹³CCN ground-state transition (Fig. 6e), an unidentified line, and feature F7. In the 90.8 GHz band, we detect the low-velocity component of a v_t=1 transition of methanol, the low-velocity component of a v₇=1 transition of HC¹³CCN (Fig. 6d and f), and the three amino acetonitrile features F8, F9, and F10. Toward the northern position P5, we detect a second velocity component of methanol v_t=1 and HC¹³CCN v₇=1 (not shown in Fig. 6, see below).

The integrated intensity maps of the amino acetonitrile features F7 to F10 in the different configurations are presented in

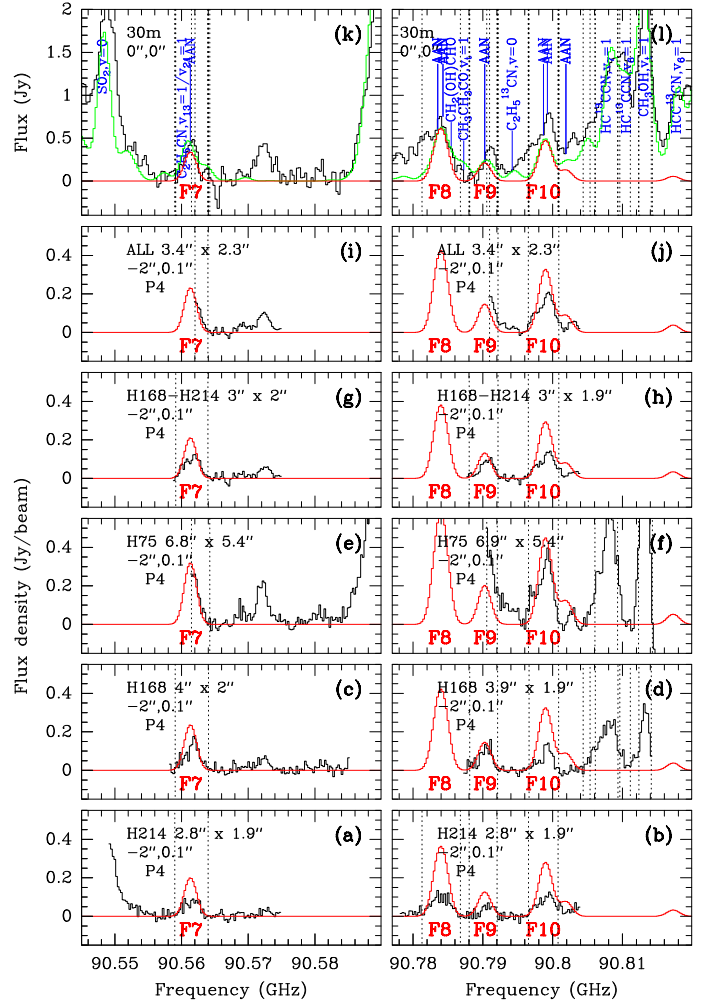


Fig. 6. Spectra obtained with the Australia Telescope Compact Array (a to j) and the 30m telescope (k and l) toward Sgr B2(N) (black histogram). The dotted lines show the frequency ranges listed in Table 7. The offset position with respect to the reference position of Fig. 7 is given in each panel. The lines identified in our 30m survey are labeled in blue. The red spectrum shows our best-fit model for amino acetonitrile (AAN) while the green spectrum corresponds to the 30m model including all molecules. The observed lines which have no counterpart in the green spectrum are still unidentified. Figures a and b show the extended configuration H 214, c and d the intermediate configuration H 168, e and f the compact configuration H 75, g and h the combination of H 214 and H 168, i and j the combination of all three configurations. The spectral coverage is not the same for all configurations because the sky tuning frequency for H 168 and H 75 was not corrected for the observatory velocity variations. The clean beam size (HPBW) is given in each panel.

Fig. 7a to p, along with maps of the excited states of methanol and HC¹³CCN (Fig. 7q to v). The frequency intervals used to compute the integrated intensities are given in Col. 3 and 4 of Table 7 and drawn in dotted lines in Fig. 6. We used the fitting routine GAUSS_2D of the GILDAS software to measure the position, size, and peak flux of each integrated emission. The results are listed in Col. 6 to 11 of Table 7. We label P4 the weighted-mean peak position of features F7 to F10, computed using the combined configuration H 214 + H 168 (only H 214 for F8), and P5 the average northern peak position of

methanol and HC^{13}CCN . The mean peak position P4 is at the offset $(-2.0 \pm 0.3'', 0.1 \pm 0.2'')$, and the average position P5 is at $(-1.9 \pm 0.1'', 5.2 \pm 0.1'')$ (see coordinates in Table 6 and positions in Fig. 7x). Finally, the ATCA velocity-integrated flux spatially integrated over the emitting region is listed in Col. 12 of Table 7 and the 30m velocity-integrated intensity is given in Col. 13.

Since the line-free frequency ranges in the two spectral windows are too small to compute a reliable continuum map, we present in Fig. 7w a map combining the emission obtained at 93.2 and 97.4 GHz in the continuum mode. The contaminating lines were avoided in the integration. The continuum emission detected with the ATCA has properties very similar to the emission detected with the PdBI (see Sect. 3.4). The emission peaks at $\alpha_{J2000} = 17^{\text{h}}47^{\text{m}}19^{\text{s}}.87 \pm 0^{\text{s}}.01$, $\delta_{J2000} = -28^{\circ}22'18.7'' \pm 0.1''$, i.e. within $0.3''$ of the ultracompact HII region K2 (Gaume et al. 1995). The continuum emission is somewhat extended around the main peak: it extends toward the other ultracompact HII regions K1, K3, and the shell-like HII region K5, but these features are not resolved with the ATCA. We also detect a shell-like emission close to K6, but its signal-to-noise ratio is lower than in the PdBI data. We do not detect any emission toward the weak ultracompact HII region K9.69 (Gaume et al. 1995).

The strong methanol $v_1=1$ and HC^{13}CCN $v_7=1$ lines show the same structure as the strong lines detected with the PdBI, namely emission from two different positions separated by about $5.1''$ in declination, each with a distinct velocity (Fig. 7q, r, t, and u). These two positions P4 and P5 coincide with the PdBI positions P1 and P2, respectively, within $0.5''$ which is about one fifth of the ATCA synthesized beam (see Fig. 7x for a visual comparison). Therefore we are very confident that they correspond to the same regions. The third position P3 detected with the PdBI in methylformate is not detected in the small number of transitions observed with the ATCA.

Within the limits of our sensitivity, the amino acetonitrile features F7 to F10 show only one peak, and they all peak at the same position P4 coincident with the PdBI position P1. *Therefore, all amino acetonitrile features detected with both the ATCA and the PdBI peak at the same position, which is consistent with their assignment to the same molecule.* The emission detected in features F7 to F10 is barely resolved with the ATCA. Given the uncertainties, it is consistent with the source size of $2''$ suggested by our measurements with the PdBI. The ATCA spatially integrated flux of feature F7 in the mixed configuration H 214 + H168 agrees with the 30m-telescope flux within 40%. Given the calibration uncertainties of both instruments, and the somewhat larger noise in the 30m spectrum, most of the flux of feature F7 is recovered with the ATCA. On the other hand, the ATCA spatially integrated fluxes of features F8 to F10 are significantly weaker than the 30m-telescope fluxes. The main reason for this disagreement may be the contamination of the 30m spectrum by emission from transitions of other molecules which are still unidentified in our survey (see Fig. 6l). This contaminating emission is missed by the interferometer either because it peaks at an offset position or because it is extended and filtered out.

The model spectrum of amino acetonitrile computed with the same parameters as the 30m model (see Table 4) but with the spatial resolution of the ATCA is shown in red in Fig. 6a to j. The agreement with the spectra obtained with the ATCA is good, within a factor of 2 (see comment about the interferometric modeling in Sect. 3.4). Overall, our LTE model of amino acetonitrile is therefore well consistent with the compact emission detected with the ATCA.

3.6. Abundance of amino acetonitrile in Sgr B2(N)

The continuum emission detected with the PdBI (see Fig. 5o) has a peak intensity of $0.459 \pm 0.009 \text{ Jy}/3.3'' \times 0.8''\text{-beam}$. In the $2''$ -diameter region convolved by the PdBI beam centered on the AAN peak position P1 (convolved FWHM: $3.9'' \times 2.2''$), we measure a mean intensity of 0.257 Jy/beam and a flux of 0.556 Jy . The continuum emission from Sgr B2(N) at 3.7 mm is dominated by thermal dust emission, at most 30% come from free-free emission (Kuan et al. 1996), probably even less toward the ultracompact HII region K2 since its flux is only 20 and 60 mJy at 2 and 1.3 cm, respectively (Gaume & Claussen 1990; Gaume et al. 1995). In addition, the thermal dust emission is optically thin (Carlstrom & Vogel 1989), so we can estimate the H_2 column density using the equation:

$$N_{\text{H}_2} = \frac{S_{\nu}^{\text{beam}}}{\Omega_{\text{beam}} \mu m_{\text{H}} \kappa_{\nu} B_{\nu}(T_{\text{dust}})}, \quad (1)$$

with S_{ν}^{beam} the intensity at $\nu = 82.0 \text{ GHz}$, $\Omega_{\text{beam}} = 7.19 \times 10^{-11} \text{ rad}^2$ the solid angle of the synthesized beam, $\mu = 2.33$ the mean molecular weight, m_{H} the mass of atomic hydrogen, κ_{ν} the dust mass opacity (for a standard gas-to-dust ratio of 100 by mass), and $B_{\nu}(T_{\text{dust}})$ the Planck function at the dust temperature T_{dust} . We assume a dust mass opacity $\kappa_{\nu}(230 \text{ GHz}) = 0.01 \text{ cm}^2 \text{ g}^{-1}$ valid for dust grains that have coagulated at high density and acquired ice mantles (Ossenkopf & Henning 1994) and a dust emissivity exponent $\beta = 1.5$, which yield a dust mass opacity $\kappa_{\nu}(82 \text{ GHz}) = 0.0036 \text{ cm}^2 \text{ g}^{-1}$. Since gas and dust are well thermally coupled via collisions at densities above $\sim 10^5 \text{ cm}^{-3}$ (see, e.g., Lesaffre et al. 2005), we assume a dust temperature equal to the excitation temperature derived for amino acetonitrile (100 K, see Table 4 and Fig. 2). We obtain a mean H_2 column density $N_{\text{H}_2} = 1.3 \times 10^{25} \text{ cm}^{-2}$ in the inner region where we detect the amino acetonitrile emission with the PdBI. Assuming a distance of 8 kpc (see Sect. 1.1), the central region of deconvolved FWHM diameter $2''$ has a linear diameter of 16000 AU. We derive a total mass of $2340 M_{\odot}$ from its integrated flux (0.556 Jy). Assuming spherical symmetry, this translates into a mean density $n_{\text{H}_2} = 1.7 \times 10^8 \text{ cm}^{-3}$.

Using the column density derived from our modeling (see Table 4), we find an amino acetonitrile abundance relative to H_2 of about 2.2×10^{-9} in the inner region of deconvolved FWHM diameter $2''$, with an uncertainty on the abundance of at least a factor of 2 given the uncertainties on the dust mass opacity and the dust emissivity exponent.

The continuum emission detected with the ATCA at a mean frequency of 95.3 GHz has a peak intensity of $1.00 \text{ Jy}/3.5'' \times 2.4''\text{-beam}$. This intensity is 1.8 times larger than the PdBI continuum flux measured over an area $3.9'' \times 2.2''$ (see above). If this flux difference comes from the frequency dependence of the continuum emission, then we derive a frequency exponent of 3.9 which is, within the calibration uncertainties, consistent with the exponent of 3.5 expected for thermal dust emission with a dust emissivity exponent $\beta = 1.5$ assumed above. We are therefore confident that the continuum emission detected toward K2 with the PdBI and the ATCA is largely dominated by thermal dust emission.

3.7. Limits on possible extended emission of cold amino acetonitrile with the VLA

Figure 8 shows the continuum image of the Sgr B2 region we obtained at 9.1 GHz with the VLA. At this frequency, the primary beam has a FWHM of $\sim 5'$. Our uv -data should adequately

Table 7. Measurements obtained toward Sgr B2(N) with the Australia Telescope Compact Array at 91 GHz.

Molecule ^a	Conf. ^b	f_{\min}^c	f_{\max}^c	σ^d	F_{peak}^e	$\Delta\alpha^e$	$\Delta\delta^e$	$\theta_{\text{maj}}^{\text{whm } e}$	$\theta_{\text{min}}^{\text{whm } e}$	P.A. ^e	Φ_{ATCA}^f	$\Phi_{30\text{m}}^g$
(1)	(2)	(MHz)	(MHz)	(Jy/beam km/s)	(6)	(")	(")	(")	(")	(°)	(Jy km/s)	(Jy km/s)
AAN F7	E	90558.99	90563.99	0.12	0.87	-2.32 ± 0.20	-0.22 ± 0.13	2.9 ± 0.4	2.2 ± 0.3	29.2 ± 0.1	1.12	3.06
AAN F7	I	90559.05	90564.05	0.15	1.47	-1.94 ± 0.20	0.58 ± 0.10	3.6 ± 0.4	2.7 ± 0.2	-79.8 ± 1.5	1.73	3.06
AAN F7	C	90561.48	90564.23	0.10	1.53	-0.96 ± 0.21	0.71 ± 0.17	7.0 ± 0.4	4.8 ± 0.3	-80.3 ± 0.0	1.37	1.79
AAN F7	M	90559.13	90563.96	0.12	1.19	-2.10 ± 0.16	0.25 ± 0.10	3.1 ± 0.3	2.7 ± 0.2	83.5 ± 0.0	1.71	2.96
AAN F7	A	90562.03	90563.96	0.06	0.61	-1.23 ± 0.15	0.26 ± 0.10	5.3 ± 0.3	3.3 ± 0.2	87.1 ± 22.5	1.37	1.00
AAN F8	E	90781.27	90786.77	0.21	1.22	-1.94 ± 0.24	-0.18 ± 0.16	3.8 ± 0.5	2.1 ± 0.3	45.0 ± 0.0	1.70	7.23
AAN F9	E	90788.02	90792.02	0.09	0.45	-1.70 ± 0.29	-0.06 ± 0.19	3.4 ± 0.6	1.9 ± 0.4	45.0 ± 0.1	0.49	2.14
AAN F9	I	90788.11	90792.11	0.13	0.97	-1.77 ± 0.26	0.23 ± 0.13	3.6 ± 0.5	2.2 ± 0.3	-84.0 ± 0.0	1.01	2.14
AAN F9	C	90790.54	90792.04	0.10	2.00	-1.25 ± 0.16	0.49 ± 0.13	6.1 ± 0.3	5.8 ± 0.3	-45.0 ± 0.0	1.86	1.59
AAN F9	M	90788.04	90792.16	0.10	0.85	-1.67 ± 0.17	0.02 ± 0.11	3.1 ± 0.3	2.4 ± 0.2	75.9 ± 0.1	1.07	2.14
AAN F9	A	90790.95	90792.16	0.05	0.63	-1.26 ± 0.14	0.23 ± 0.09	4.8 ± 0.3	3.9 ± 0.2	84.5 ± 0.0	1.51	1.31
AAN F10	E	90796.52	90800.77	0.16	1.17	-2.51 ± 0.20	0.02 ± 0.13	2.7 ± 0.4	2.2 ± 0.3	-81.2 ± 0.2	1.38	6.48
AAN F10	I	90796.61	90800.86	0.10	0.93	-1.81 ± 0.21	0.20 ± 0.11	3.3 ± 0.4	2.0 ± 0.2	82.3 ± 0.0	0.79	6.19
AAN F10	C	90796.54	90800.79	0.15	3.36	-1.08 ± 0.15	0.28 ± 0.12	6.6 ± 0.3	4.9 ± 0.2	-77.7 ± 0.0	2.78	6.48
AAN F10	M	90796.52	90800.88	0.13	1.32	-2.28 ± 0.15	0.03 ± 0.09	2.9 ± 0.3	2.2 ± 0.2	83.7 ± 22.5	1.42	6.48
AAN F10	A	90796.52	90800.88	0.13	1.82	-1.66 ± 0.12	0.12 ± 0.08	4.5 ± 0.2	3.1 ± 0.2	-89.3 ± 22.5	3.24	6.48
HC ¹³ CCN $v_7=1$ HV	I	90804.36	90805.36	0.05	0.49	-1.94 ± 0.20	5.16 ± 0.10	3.0 ± 0.4	2.0 ± 0.2	84.4 ± 0.0	0.41	2.39
HC ¹³ CCN $v_7=1$ LV	I	90806.11	90809.36	0.14	2.74	-1.56 ± 0.10	0.55 ± 0.05	3.7 ± 0.2	2.1 ± 0.1	83.6 ± 0.0	2.69	10.30
HC ¹³ CCN $v_7=1$ LV	C	90806.04	90809.29	0.15	4.98	-1.71 ± 0.10	0.25 ± 0.08	7.1 ± 0.2	4.4 ± 0.2	-83.8 ± 0.0	4.12	10.30
CH ₃ OH $v_t=1$ HV	I	90809.61	90811.11	0.09	1.52	-1.85 ± 0.12	5.23 ± 0.06	3.7 ± 0.2	2.1 ± 0.1	-85.7 ± 0.1	1.54	6.55
CH ₃ OH $v_t=1$ LV	I	90812.36	90814.11	0.11	1.60	-1.84 ± 0.13	0.44 ± 0.06	3.8 ± 0.3	3.6 ± 0.1	23.7 ± 22.5	2.72	10.40
CH ₃ OH $v_t=1$ LV	C	90812.29	90814.29	0.12	5.22	-1.86 ± 0.08	-0.03 ± 0.06	7.1 ± 0.2	4.5 ± 0.1	-77.9 ± 0.0	4.29	10.40

- (a) For amino acetonitrile (AAN), we give the feature number like in Col. 8 of Table 3. For the other molecules, HV and LV mean high and low velocity component, respectively.
- (b) Interferometer configuration: E: extended (H 214), I: intermediate (H 168), C: compact (H 75), M: mixed (H 214 + H 168), A: all (H 214 + H 168 + H 75).
- (c) Frequency range over which the intensity was integrated.
- (d) Noise level in the integrated intensity map shown in Fig. 7.
- (e) Peak flux, offsets in right ascension and declination with respect to the reference position of Fig. 7, major and minor diameters (FWHM), and position angle (East from North) derived by fitting an elliptical 2D Gaussian to the integrated intensity map shown in Fig. 7. The uncertainty in Col. 11 is the formal uncertainty given by the fitting routine GAUSS_2D, while the uncertainties correspond to the beam size divided by two times the signal-to-noise ratio in Col. 7 and 8 and by the signal-to-noise ratio in Col. 9 and 10.
- (f) Flux spatially integrated over the region showing emission in the integrated intensity map of Fig. 7.
- (g) Integrated flux of the 30m spectrum computed over the frequency range given in Col. 3 and 4.

sample structures with sizes of up to 1.5'. There are two major continuum sources, Sgr B2(N) and (M), whose emission is a blend of the contributions of many separate sources that are resolved in higher resolution images (e.g., Gaume et al. 1995). A number of secondary sources are evident. The peak brightness, S_p , toward Sgr B2(N) is 2.85 Jy beam⁻¹. Toward Sgr B2(M) we measure $S_p = 4.12$ Jy beam⁻¹. The image has a relatively high 1σ rms noise level of 8.4 mJy beam⁻¹ that is determined by dynamic range limitations. Nowhere in the whole line datacube do we find any significant line emission or absorption above 3.4 mJy beam⁻¹ (5 times the 1σ rms noise level in the images of the spectral line emission). This corresponds to a brightness temperature upper limit of 0.35 K. With this, and assuming a width of 30 km s⁻¹, similar to other lines with extended emission (e.g., Hunt et al. 1999; Hollis et al. 2004) we can use the standard relation to calculate an upper limit to the column densities of the upper levels of the strongest of the $J_{K_a, K_c} = 1_01 - 0_00$ hfs components of $\sim 8 \times 10^{12}$ cm⁻². Hollis et al. (2004) use a two temperature component picture to explain their multitransition glycolaldehyde study, invoking components with temperatures of $T = 8$ and 50 K. For 8 K, our limit on the total column density of extended amino acetonitrile would be $\sim 3 \times 10^{14}$ cm⁻² and for 50 K it would be $\sim 3 \times 10^{16}$ cm⁻². The low- T value is

on the same order as the total column density of glycolaldehyde that Hollis et al. (2004) calculate for this temperature.

Using the ATCA, Hunt et al. (1999) imaged Sgr B2 in the $J = 1 - 0$ line of HC₃N at a frequency near 9.1 GHz, very close to our amino acetonitrile frequency. In their 4.4" × 9.9" resolution images they found the spatial distribution of the line emission to resemble that of the continuum emission very closely. Assuming that possible extended amino acetonitrile had a similar distribution, the high continuum flux densities allow us to determine very sensitive limits on possible absorption (or weakly inverted emission) toward the continuum emission. We calculate very low 5σ limits on the absolute value of the optical depth of 8.3×10^{-4} and 1.2×10^{-3} toward Sgr B2(N) and (M). This implies ~ 125 and 20 times lower column density limits for $T = 8$ and 50 K, respectively, compared to limits on possible thermal emission quoted above.

4. Discussion

4.1. Amino acetonitrile in Sgr B2(N)

We detected compact emission from amino acetonitrile in Sgr B2(N) with a source size of 2" FWHM, a column density of 2.8×10^{16} cm⁻², an excitation temperature of 100 K, a linewidth of 7 km s⁻¹, and a centroid velocity of 64 km s⁻¹ (see

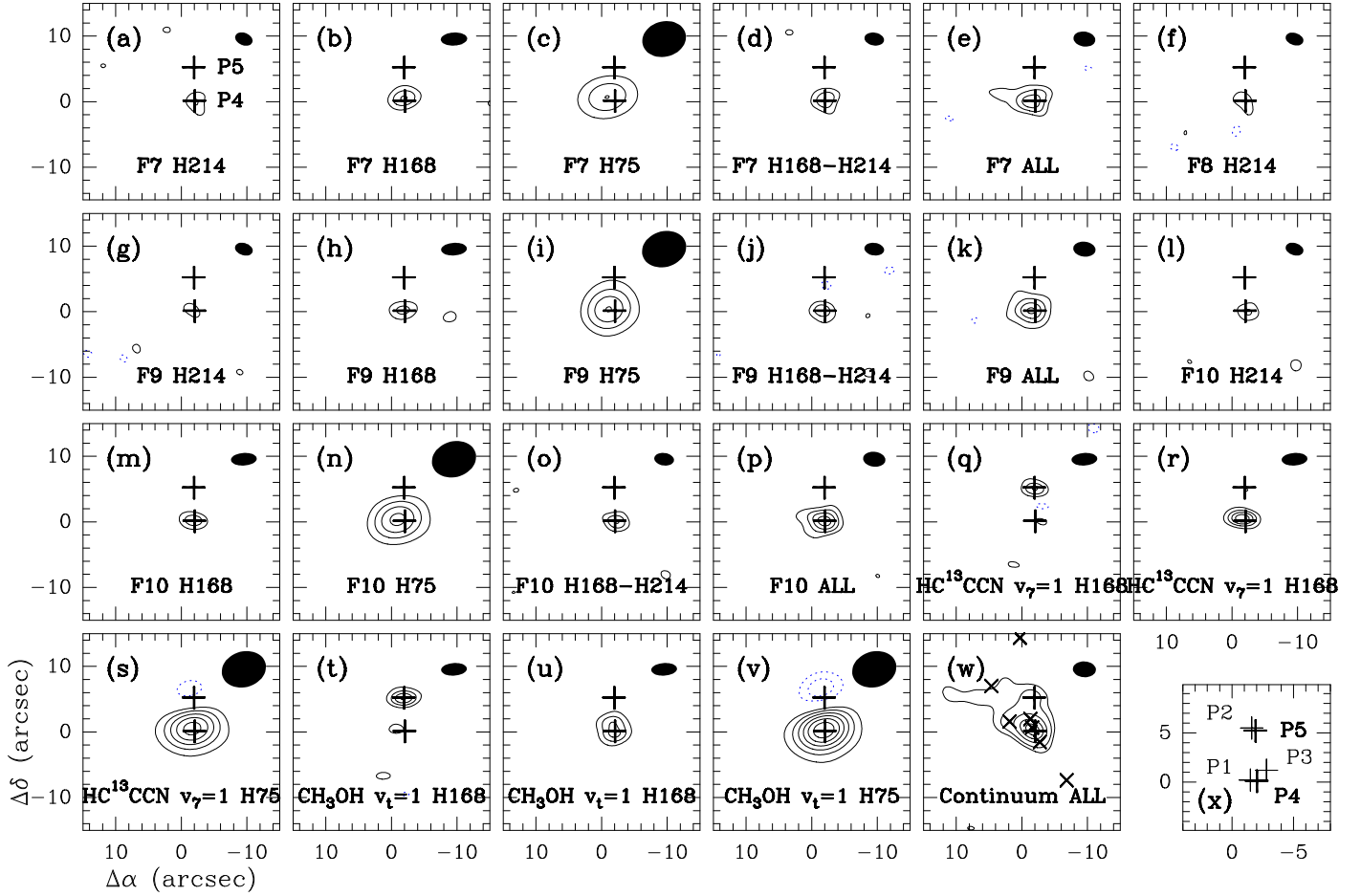


Fig. 7. Integrated intensity maps (panels **a** to **v**) and continuum map (panel **w**) obtained toward Sgr B2(N) with the Australia Telescope Compact Array at 3 mm. Panels (**a**) to (**p**) show the amino acetonitrile features F7 to F10 in the different configurations (see Fig. 6). Panels **q** to **v** show the other molecules listed in Table 3. The lower contour (positive in black solid line and negative in blue dotted line) and the contour step are 3σ for panels **a**, **b**, **d** to **h**, **j** to **m**, and **o** to **q**, 4σ for panels **r**, **t**, and **u**, 5σ for panels **c**, **i** and **n**, and 6σ for panels **s** and **v** (with σ given in Col. 5 of Table 7). For panel **w**, the first contours are 3 and 6σ , and the contour step is 6σ for the other contours (with $\sigma = 37$ mJy/beam). In each panel, the 0,0 position is $\alpha_{J2000} = 17^{\text{h}}47^{\text{m}}20^{\text{s}}.00$, $\delta_{J2000} = -28^{\circ}22'19.0''$, the two thick plus symbols mark positions P4 and P5 (labeled in panel **a**), and the filled ellipse in the top right corner shows the clean beam. The cross symbols in panel **w** are the peak positions of the (ultracompact) HII regions detected by Gaume et al. (1995) at 1.3 cm (K9.69, and K1 to K6, from right to left). The spectral integration was done on the frequency ranges given in Table 7. The maps are not corrected for primary beam attenuation. Panel **x** displays the ATCA positions P4 and P5 with thick plus symbols and the PdBI positions P1 to P3 with thin plus symbols, for visual comparison.

Table 4). We estimated the abundance of amino acetonitrile to be 2.2×10^{-9} in this compact region. We found no evidence for a possible colder, more extended emission. The compact emission peaks at position P1 (see Sect. 3.4 and Table 6), which is located $0.4''$ South of the ultracompact HII region K2 where the 3.7 mm thermal dust continuum emission detected with the PdBI also peaks. This angular separation is at a level of 2σ only, so it may not be significant. Our PdBI and ATCA data show that ethyl cyanide $\text{C}_2\text{H}_5\text{CN}$, cyanoacetylene HC_3N in its excited states $v_7 = 1$ and $v_4 = 1$, HC^{13}CCN in its excited state $v_7 = 1$, and methanol CH_3OH in its excited state $v_t = 1$ also peak at this position P1. The amino acetonitrile emission arises therefore from the hot core region called the “Large Molecule Heimat” (see Sect. 1.1.2). Our PdBI continuum data show that this compact region is extremely dense ($1.7 \times 10^8 \text{ cm}^{-3}$) and massive ($2340 M_{\odot}$). The ultracompact HII region K2 is most likely still embedded in the dense, hot core traced by the thermal dust emission and seems therefore to be the youngest source among the numerous ultracompact HII regions populating the Sgr B2 molecular cloud.

In addition, the LMH hosts the powerful Sgr B2(N) H_2O maser region. The distribution of the maser emission over $4'' \times 2''$ was mapped using Very Long Baseline Interferometry by Reid et al. (1988), who also fitted a kinematical model invoking expansion and rotation. The best fit center of expansion is displaced from our interferometric position P1 by $(\Delta\alpha, \Delta\delta) = (-0.49'', -0.66'')$, which is less than the combined positional uncertainty of the VLBI and PdBI data. The best fit radial component of the expansion velocity, $63 \pm 3 \text{ km s}^{-1}$, is also in excellent agreement with the 64 km s^{-1} that we obtain for the LMH (see Table 4). H_2O masers are associated with young stellar objects in their earliest stages when they drive powerful outflows, such as the one found in Sgr B2(N) which has a total velocity extent of $\sim \pm 50 \text{ km s}^{-1}$ (see, e.g., Reid et al. 1988). Thus, the water vapor maser provides evidence for the youth of the LMH, the very compact region where the amino acetonitrile emission originates from.

Bisschop et al. (2007) measured the abundances of various complex molecules in massive hot core regions and classified these molecules as “cold” ($< 100 \text{ K}$) or “hot” ($> 100 \text{ K}$).

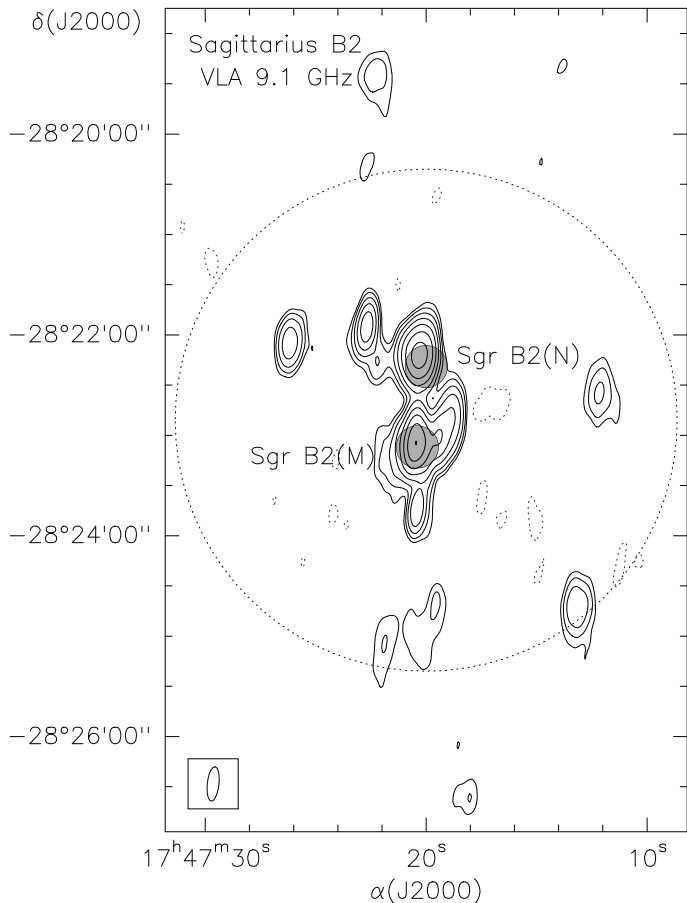


Fig. 8. Continuum image of the Sgr B2 region obtained with the Very Large Array at 9.1 GHz. The lowest contour level is 4 times the rms noise level of 8 mJy beam^{-1} and contours double in value until they reach 512 times that level. The dotted circle represents the FWHM of the VLA antennas' primary beam at 9.1 GHz. The image is not corrected for attenuation due to the primary beam's response. Note that it is produced from data taken over only a 1 hour period and has limited dynamic range and sensitivity. It is, however, consistent with the higher sensitivity three-pointing-mosaic 4.8 GHz image presented by Mehringer et al. (1995), which has a similar resolution. The synthesized beam is represented in the lower left corner. The upper and lower shaded circles are centered at the Sgr B2(N) and (M) pointing positions of our 30m telescope spectral line survey, respectively. Their size corresponds to the $25''$ FWHM of the 30m telescope at 100 GHz.

Based on the high abundances, the similar high rotation temperatures, and the relative constant abundance ratios of the oxygen-bearing species and two nitrogen-bearing species, they concluded that the “hot” molecules share a common solid state formation scheme. From an analysis of the emission of complex organic molecules in molecular clouds in the Galactic center region and a comparison to results previously obtained in hot cores, Requena-Torres et al. (2006) support also the scenario in which complex organic molecules are formed on the grain surfaces. The high temperature and abundance we measured for amino acetonitrile suggest it shares the same properties as the “hot” molecules found by Bisschop et al. (2007), which favors its formation on the grain surfaces, although its detection in other hot cores to check if it follows the abundance correlations found by Bisschop et al. (2007) and Requena-Torres et al. (2006) is needed to prove this conclusion.

Wirström et al. (2007) failed to detect amino acetonitrile in the hot cores Orion KL, W51 e1/e2, S140, and W3(OH) with the Onsala 20m telescope. They found *beam-averaged* column density upper limits of $1.1 - 3.5 \times 10^{13} \text{ cm}^{-2}$ for amino acetonitrile, while they detected vinylcyanide $\text{C}_2\text{H}_3\text{CN}$ with a column density of $\sim 2 \times 10^{14} \text{ cm}^{-2}$ in the first two sources. Our 30m observations of Sgr B2(N) imply a column density of $8 \times 10^{17} \text{ cm}^{-2}$ for vinylcyanide with a source size of $2.3''$ (Belloche et al., *in prep.*), i.e. about 30 times our amino acetonitrile column density. If the column density ratio of these two species in Sgr B2(N) holds for other hot cores, then the observations of Wirström et al. (2007) were not sensitive enough to detect amino acetonitrile in their sources.

Our PdBI and ATCA data show that the double peak structure seen in many transitions detected with the 30m telescope are produced by two sources separated by about $5.3''$ in the North-South direction (positions P1 and P2, see Sect. 3.4). The centroid velocity difference between these two positions is about 9 km s^{-1} . The northern and more redshifted source (P2) is about twice weaker in the molecular emission detected in our 30m data (Belloche et al., *in prep.*). These two sources were already detected in ethylcyanide with high-resolution observations (see, e.g., Liu & Snyder 1999; Hollis et al. 2003; Jones et al. 2007). Our interferometric data show that cyanoacetylene HC_3N and its isotopologue HC^{13}CCN in their excited state $v_7 = 1$, and methanol in its excited state $v_t = 1$ are also detected toward both sources. In the PdBI spectra shown in Fig. 4c and d, we do not find a clear evidence for amino acetonitrile at a velocity of $\sim 73 \text{ km s}^{-1}$. There may be a hint of emission at a level about a factor of 2 lower than the emission toward P1 (see also Feature F3 in the 30m spectrum in Fig. 4g), but it is below our 3σ detection limit. Therefore we *cannot rule out* that amino acetonitrile shares the same property as, e.g., ethylcyanide, cyanoacetylene, and methanol and is also present in the northern source P2 at a level about twice lower than in P1.

The molecular source P2 is not detected at a 3σ level of $26 \text{ mJy}/3.4'' \times 0.81''$ -beam in the continuum map we obtained with the PdBI at 82.0 GHz (see Fig. 5o). On the other hand, we detect some emission with an intensity of $280 \text{ mJy}/3.5'' \times 2.4''$ -beam in the continuum map obtained with the ATCA at a mean frequency of 95.3 GHz (see Fig. 7w). If this emission is more extended than the PdBI beam, then the PdBI upper limit translates into 79 mJy in the ATCA beam, which yields an unphysical frequency exponent of ~ 8 for the continuum emission toward P2 (see Sect. 3.6). We suspect that the ATCA continuum toward P2 is contaminated by a low-level line emission. In any case, since the continuum emission toward P2 is much weaker than toward P1 at 3mm, P2 must be less dense and/or less hot than the hot core P1. P2 coincides with a weak blob of emission in the 1.3 cm VLA map of Gaume et al. (1995) (see their Fig. 6 and 7). However, this blob is located within the shell-like, weak, extended emission associated with K5 and it is difficult to know if it is compact or not from the 1.3 cm map published by these authors. Therefore the hot core P2 traced by the molecular emission may also be associated with an ultracompact HII region, weaker than K2. Alternatively, if it is not directly associated with a compact source of free-free emission, it may have been formed by the interaction of the shell-like structure K5 with the ambient medium, and could be in an earlier stage of evolution than the hot core P1 (LMH) associated with the ultracompact HII region K2.

4.2. Amino acetonitrile in Sgr B2(M)

We do not detect amino acetonitrile in our 30m survey toward Sgr B2(M). Using the same parameters as for Sgr B2(N) (100 K and a FWHM source size of $2''$), we find a $\sim 3\sigma$ column density upper limit of $6 \times 10^{15} \text{ cm}^{-2}$ in the LTE approximation. The column density of amino acetonitrile is thus at least a factor ~ 5 weaker toward Sgr B2(M) than toward Sgr B2(N). This is not surprising since, e.g., Nummelin et al. (2000) found that hot-core-type molecules are more abundant in Sgr B2(N) by factors 3–8 as compared to Sgr B2(M).

4.3. Amino acetonitrile, a precursor of glycine?

Amino acids, building blocks of proteins and therefore key ingredients to explain the origin of life, have been found in meteorites on Earth. Their deuterium isotopic composition suggests that they, or at least their direct precursors, were formed in the cold interstellar medium (e.g. Pizzarello & Huang 2005). Looking for amino acids in the interstellar medium is therefore appealing. However, the simplest amino acid glycine has been intensively searched for in the past 30 years, but has unfortunately not been discovered yet (e.g. Brown et al. 1979; Snyder et al. 2005; Cunningham et al. 2007).

Amino acetonitrile was proposed early on as a possible direct precursor of glycine in the interstellar medium (e.g. Brown et al. 1977). The formation of glycine via a Strecker-cyanohydrin synthesis has long been favored (Peltzer et al. 1984; Ehrenfreund et al. 2001; Bernstein et al. 2004). This pathway involves a carbonyl compound (such as an aldehyde or a ketone), hydrogen cyanide, and ammonia, and produces the amino nitrile which, after hydrolysis, yields the amino acid. However, the Strecker synthesis cannot explain the higher deuterium fractionation of amino acids compared to hydroxy acids which was measured in meteorites (see Elsila et al. 2007 and references therein).

Amino acids were successfully produced in the laboratory by UV-photolysis of ice mixtures mimicking the mantles of interstellar grains (Bernstein et al. 2002; Muñoz Caro et al. 2002). For an ice mixture composed of H_2O , CH_3OH , NH_3 , and HCN , Woon (2002) proposed theoretically a pathway of radical-radical reactions involving the radicals t-HOCO and CH_2NH_2 produced by UV irradiation. This hypothesis was tested and verified experimentally by Holtom et al. (2005) with an ice mixture of CH_3NH_2 and CO_2 bombarded by energetic electrons mimicking the impact of cosmic rays in the interstellar medium. This pathway leading to glycine does not involve the formation of amino acetonitrile. On the other hand, Elsila et al. (2007) experimented the UV-photolysis of an ice mixture of H_2O , CH_3OH , HCN , and NH_3 , and found with isotopic labeling techniques multiple pathways leading to the formation of amino acids. The main pathway involves the formation of the amino nitrile and they proposed “a modified radical-radical mechanism that takes into account the formation of nitriles as amino acid precursor molecules”. They also noticed that a Strecker-type synthesis may be at most a minor contributor to the formation of glycine.

The formation of glycine in the gas phase was also investigated. Blagojevic et al. (2003) synthesized ionized glycine via the reaction of the hydroxylamine ion NH_2OH^+ with acetic acid CH_3COOH . They proposed the formation of the precursor hydroxylamine NH_2OH in the grain mantles and the formation of acetic acid via ion-molecule reactions in the gas phase. Based on quantum chemical calculations, Maeda & Ohno (2006) found another pathway to form glycine in the gas phase involving bar-

rierless reactions between closed-shell species. Their pathway starts from CO_2 , NH_3 , and CH_2 , and leads to glycine via the reaction of CO_2 with the closed-shell molecule CH_2NH_3 , a higher energy isomer of methylamine CH_3NH_2 . However, they mentioned that CH_2NH_3 should be efficiently destroyed by H_2O , so this pathway may be unlikely in the interstellar gas phase where water can be very abundant. Both gas phase formation routes do not involve amino acetonitrile as a direct precursor of glycine.

This brief overview of the experimental and theoretical work on the formation of amino acids in the interstellar medium shows that there is no consensus about the chemical precursors of amino acids. It is however important to note that the amino acids produced in the ice experiments mentioned above (except Holtom et al. 2005) are found experimentally *after* the hydrolysis of the ice residues. It is possible that only their precursors (e.g. amino nitriles) are synthesized by the ice photochemistry, and that the amino acids are formed only later, e.g. on the comet/asteroids surfaces, by hydrolysis (Elsila et al. 2007). Therefore amino acetonitrile may well be a direct precursor of glycine.

The formation of amino acetonitrile itself was also investigated theoretically by Koch et al. (2008). They found that water can efficiently catalyze a reaction between methylenimine CH_2NH and hydrogen isocyanide HNC to form amino acetonitrile in the grain mantles at a temperature of 50 K. Methylenimine was detected in the gas phase toward Sgr B2(N) by, e.g., Nummelin et al. (2000). They found evidence for both hot, compact and cold, extended components and derived a column density of $3.3 \times 10^{17} \text{ cm}^{-2}$ for the compact component, with a source size of $2.7''$ and a temperature of $210^{+400}_{-80} \text{ K}$, which is consistent with our own analysis (Belloche et al., *in prep.*). This column density is an order of magnitude larger than the column density we derived for amino acetonitrile, which does not rule out methylenimine as a precursor of amino acetonitrile.

4.4. Glycine in Sgr B2(N)

The frequency coverage of our 30m survey of Sgr B2(N) includes many transitions of glycine as listed in the CDMS catalog (entries 75511 and 75512), but we do not detect this molecule within the limits of our LTE analysis. Using the same parameters as for amino acetonitrile (100 K and a source size of $2''$, see Table 4), we derive a column density upper limit of $2.0 \times 10^{17} \text{ cm}^{-2}$ for conformer I and $5.0 \times 10^{15} \text{ cm}^{-2}$ for conformer II. Alternatively, the upper limit on emission from glycine more extended than the 30m beam at 3mm ($\sim 26''$) is $1.2 \times 10^{15} \text{ cm}^{-2}$ for conformer I and $3.0 \times 10^{13} \text{ cm}^{-2}$ for conformer II. For a temperature of 75 K, we find column density upper limits for conformer I of $1.5 \times 10^{17} \text{ cm}^{-2}$ for a source size of $2''$ and $8.9 \times 10^{14} \text{ cm}^{-2}$ for emission more extended than the 30m beam, and for conformer II $3.7 \times 10^{15} \text{ cm}^{-2}$ and $2.2 \times 10^{13} \text{ cm}^{-2}$, respectively.

Jones et al. (2007) did not detect glycine conformer I in Sgr B2(N) with the ATCA and derived a 3σ upper limit of $1.4 \times 10^{15} \text{ cm}^{-2}$ for the beam-averaged column density at 75 K, which translates into an upper limit of $2.0 \times 10^{16} \text{ cm}^{-2}$ for a source size of $2''$ after correction for beam dilution ($17.0'' \times 3.4''$). This upper limit on any compact emission from glycine is at a level 8 times lower than the one we derive with the 30m telescope. As Jones et al. (2007) mentioned, the tentative detection of Kuan et al. (2003) is *inconsistent* with this upper limit in the case of compact emission. On the other hand, the ATCA non-detection does not exclude extended emission at the level found by Kuan et al. (2003) who reported a beam-averaged column

density of $4.2 \times 10^{14} \text{ cm}^{-2}$ with the NRAO 12m telescope and a rotational temperature of 75 K. However Cunningham et al. (2007) did not detect glycine conformer I in Sgr B2(N) with the 22m Mopra telescope and derived a 3σ upper limit of $3.7 \times 10^{14} \text{ cm}^{-2}$ for the beam-averaged column density at 75 K. This upper limit is at a level 2.4 times lower than our beam-averaged upper limit. However, their upper limit was derived for a position offset by $26''$ from the hot core position, so it only rules out emission from Sgr B2(N) more extended than $\sim 50''$ in diameter. If glycine's emission were centered on the hot core position with a diameter of $\sim 25''$, Mopra would have missed $\sim 80\%$ of the flux, and their upper limit would be $1.9 \times 10^{15} \text{ cm}^{-2}$. In that case, our upper limit is more significant, but not low enough to rule out the tentative detection reported by Kuan et al. (2003) if glycine is confined to a source size of $\sim 30''$. However, the arguments presented by Snyder et al. (2005) do rule out this case. As a conclusion, the upper limits of Cunningham et al. (2007), Jones et al. (2007), and Snyder et al. (2005) rule out emission of glycine conformer I at the level reported by Kuan et al. (2003) in Sgr B2(N) for any source size.

Cunningham et al. (2007) found an upper limit of $7.7 \times 10^{12} \text{ cm}^{-2}$ for the beam-averaged column density of glycine conformer II with Mopra toward the central position of Sgr B2(N). This upper limit is nearly a factor of 3 lower than the upper limit we derived above with the 30m telescope for extended emission. With the ATCA, Jones et al. (2007) found an upper limit of $8.6 \times 10^{13} \text{ cm}^{-2}$ for the beam-averaged column density, which translates into $1.2 \times 10^{15} \text{ cm}^{-2}$ for a source size of $2''$. This upper limit is again a factor of 3 lower than the upper limit we derived above with the 30m telescope for compact emission.

Bernstein et al. (2004) found experimentally that organic acids are less stable than organic nitriles against UV photodestruction but they concluded that in dense molecular clouds, the ratio nitrile to acid should be affected by less than a factor of 2 over the lifetime of the cloud. Therefore it could be instructive to compare the pairs methylcyanide/acetic acid ($\text{CH}_3\text{CN}/\text{CH}_3\text{COOH}$) and amino acetonitrile/glycine ($\text{NH}_2\text{CH}_2\text{CN}/\text{NH}_2\text{CH}_2\text{COOH}$). In our 30m line survey (Belloche et al., *in prep.*), we derive a column density ratio on the order of 200 for $\text{CH}_3\text{CN}/\text{CH}_3\text{COOH}$ toward Sgr B2(N). If the two pairs are produced by similar chemical pathways yielding similar column density ratios, then we expect the glycine column density to be two orders of magnitude smaller than the amino acetonitrile column density, i.e. about $2 \times 10^{14} \text{ cm}^{-2}$ for a compact source of $2''$ diameter, which is nearly two orders of magnitude smaller than the upper limit derived above for glycine conformer I from the ATCA measurements of Jones et al. (2007), and a factor 5 smaller for conformer II. Therefore glycine emission may be well below the confusion limit in Sgr B2(N).

5. Conclusions

We used the complete 3 mm and partial 2 and 1.3 mm line surveys obtained with the IRAM 30m telescope toward the hot cores Sgr B2(N) and (M) to search for emission from the complex molecule amino acetonitrile. We carried out follow-up observations with the IRAM Plateau de Bure and ATCA interferometers at selected frequencies. We also looked for extended emission from cold amino acetonitrile with the VLA. We report the detection of amino acetonitrile toward the hot core Sgr B2(N)-LMH, which is the first detection of this molecule in the interstellar medium. Our main results and conclusions are the following:

1. In the course of this work, we prepared an amino acetonitrile entry (56507) for the catalog of the Cologne Database for Molecular Spectroscopy (CDMS) using the laboratory transition frequencies reported by Bogey et al. (1990).
2. 88 of the 398 significant transitions of amino acetonitrile covered by our 30m line survey are relatively free of contamination from other molecules and are detected in the form of 51 observed features toward Sgr B2(N).
3. Nine features out of 51 were followed-up upon and detected with the IRAM PdB and ATCA interferometers. The amino acetonitrile emission looks compact and we derive a source size of about $2''$ in diameter (FWHM).
4. With a source size of $2''$ and an LTE analysis, we derive an amino acetonitrile column density of $2.8 \times 10^{16} \text{ cm}^{-2}$ for a temperature of 100 K and a linewidth of 7 km s^{-1} .
5. The compact continuum emission detected with the PdB interferometer yields a mean H_2 column density $N_{\text{H}_2} = 1.3 \times 10^{25} \text{ cm}^{-2}$ in the central region of diameter $2''$ for a temperature of 100 K, which implies a mean density $n_{\text{H}_2} = 1.7 \times 10^8 \text{ cm}^{-3}$, a mass of $2340 M_{\odot}$, and an amino acetonitrile fractional abundance of 2.2×10^{-9} .
6. The high abundance and temperature may indicate that amino acetonitrile is formed by grain surface chemistry.
7. We detected emission from ethylcyanide $\text{C}_2\text{H}_5\text{CN}$, cyanoacetylene HC_3N and its isotopologue HC^{13}CCN in their $v_7=1$ excited states, and methanol CH_3OH in its excited state $v_t=1$ in two compact sources toward Sgr B2(N). The two sources are separated by about $5.3''$ in the North-South direction and by 9 km s^{-1} in velocity. They produce double peaked line shapes for many molecules detected in our 30m line survey. Only the southern source is detected with the PdBI in continuum emission. It is associated with the ultracompact HII region K2 and a powerful H_2O maser region, and must be very young. The northern source is weaker in molecular emission and must be less dense and/or less hot. It may be associated with a weaker ultracompact HII region and may be in an even earlier stage of evolution. The sensitivity of our observations was not good enough to detect amino acetonitrile toward the northern source. It is at least a factor of 2 weaker than toward the southern source.
8. We did not detect amino acetonitrile toward Sgr B2(M) and derived a column density upper limit of $6 \times 10^{15} \text{ cm}^{-2}$.
9. We failed to detect any extended emission from cold amino acetonitrile with the VLA and derived a column density upper limit of $3 \times 10^{12-14} \text{ cm}^{-2}$ at 8 K.
10. Amino acetonitrile may be a chemical precursor of glycine. We did not detect the glycine conformers I and II in our 30m line survey. The column density upper limits we derive are less constraining than upper limits previously published by other authors. Based on our detection of amino acetonitrile and a comparison to the pair methylcyanide/acetic acid ($\text{CH}_3\text{CN}/\text{CH}_3\text{COOH}$) both of which are detected in our survey, we conclude that the column density of glycine conformers I and II in Sgr B2(N) may be two orders of magnitude and a factor 5 below the current best upper limits, respectively, which would be below the confusion limit of Sgr B2(N) in the 1–3 mm range.

Acknowledgements. We thank the IRAM staff in Grenoble for observing at the PdBI and for their help with the data reduction, the IRAM staff in Granada for service observing in January 2005, and Sergio Martin for providing the reference (off) position for our 30m observations. We thank John Pearson for his predictions of the first excited state of ethylcyanide, Claus Nielsen for providing transition frequencies of formamide isotopologues, Isabelle Kleiner, Vadim Ilyushin, and Frank Lovas for acetic acid frequencies, and Brian Drouin for his predictions of acetone. H. S. P. M. and the CDMS had been supported initially through the

Deutsche Forschungsgemeinschaft (DFG) via the collaborative research grant SFB 494. Recent support is provided by the Bundesministerium für Bildung und Forschung administered through Deutsches Zentrum für Luft- und Raumfahrt (DLR; the German space agency). J. O. is a Jansky Fellow of the National Radio Astronomy Observatory. C. H. is a fellow of the Studienstiftung des deutschen Volkes and member of the International Max-Planck Research School for Radio and Infrared Astronomy.

References

- Bernstein, M. P., Dworkin, J. P., Sandford, S. A., Cooper, G. W., & Allamandola, L. J. 2002, *Nature*, 416, 401
- Bernstein, M. P., Ashbourn, S. F. M., Sandford, S. A., & Allamandola, L. J. 2004, *ApJ*, 601, 365
- Berulis, I. I., Winnewisser, G., Krasnov, V. V., & Sorochenko, R. L. 1985, *Soviet Astronomy Letters*, 11, 251
- Bisschop, S. E., Jörgensen, J. K., van Dishoeck, E. F., & de Wachter, E. B. M. 2007, *A&A*, 465, 913
- Blagojevic, V., Petrie, S., & Bohme, D. K. 2003, *MNRAS*, 339, L7
- Bogey, M., Dubus, H., & Guillemin, J. C. 1990, *J. Mol. Spectrosc.*, 143, 180
- Brown, R. D., Godfrey, P. D., Ottrey, A. L., & Storey, J. W. V. 1977, *J. Mol. Spectrosc.*, 68 (3), 359
- Brown, R. D., Godfrey, P. D., Storey, J. W. V., Bassez, M.-P., et al. 1979, *MNRAS*, 186, 5P
- Carlstrom, J. E., & Vogel, S. N. 1989, *ApJ*, 337, 408
- Clark, B. G. 1980, *A&A*, 89, 377
- Ceccarelli, C., Loinard, L., Castets, A., Faure, A., & Lefloch, B. 2000, *A&A*, 362, 1122
- Combes, F., Q-Rieu, N., & Wlodarczak, G. 1996, *A&A*, 308, 618
- Comito, C., Schilke, P., Phillips, T. G., Lis, D. C., Motte, F., & Mehringer, D. 2005, *ApJS*, 156, 127
- Cummins, S. E., Linke, R. A., & Thaddeus, P. 1986, *ApJS*, 60, 819
- Cunningham, M. R., et al. 2007, *MNRAS*, 376, 1201
- Dahmen, G., et al. 1997, *A&AS*, 126, 197
- de Vicente, P., Martín-Pintado, J., Neri, R., & Colom, P. 2000, *A&A*, 361, 1058
- Ehrenfreund, P., Glavin, D. P., Botta, O., Cooper, G., & Bada, J. L. 2001, *Proceedings of the National Academy of Science*, 98, 2138
- Eisenhauer, F., Schödel, R., Genzel, R., Ott, T., Tecza, M., Abuter, R., Eckart, A., & Alexander, T. 2003, *ApJ*, 597, L121
- Elsila, J. E., Dworkin, J. P., Bernstein, M. P., Martin, M. P., & Sandford, S. A. 2007, *ApJ*, 660, 911
- Gaume, R. A., & Claussen, M. J. 1990, *ApJ*, 351, 538
- Gaume, R. A., Claussen, M. J., de Pree, C. G., Goss, W. M., & Mehringer, D. M. 1995, *ApJ*, 449, 663
- Goldsmith, P. F., & Langer, W. D. 1999, *ApJ*, 517, 209
- Gordy, W., & Cook, R. L. 1984, *Microwave Molecular Spectra*, 3rd edition, Wiley (New York)
- Hollis, J. M., Snyder, L. E., Suenram, R. D., & Lovas, F. J. 1980, *ApJ*, 241, 1001
- Hollis, J. M., Lovas, F. J., & Jewell, P. R. 2000, *ApJ*, 540, L107
- Hollis, J. M., Vogel, S. N., Snyder, L. E., Jewell, P. R., & Lovas, F. J. 2001, *ApJ*, 554, L81
- Hollis, J. M., Lovas, F. J., Jewell, P. R., & Coudert, L. H. 2002, *ApJ*, 571, L59
- Hollis, J. M., Pedelty, J. A., Boboltz, D. A., Liu, S.-Y., Snyder, L. E., Palmer, P., Lovas, F. J., & Jewell, P. R. 2003, *ApJ*, 596, L235
- Hollis, J. M., Jewell, P. R., Lovas, F. J., Remijan, A., & Møllendal, H. 2004, *ApJ*, 610, L21
- Hollis, J. M., Jewell, P. R., Remijan, A. J., & Lovas, F. J. 2007, *ApJ*, 660, L125
- Holtom, P. D., Bennett, C. J., Osamura, Y., Mason, N. J., & Kaiser, R. I. 2005, *ApJ*, 626, 940
- Hunt, M. R., Whiteoak, J. B., Cragg, D. M., White, G. L., & Jones, P. A. 1999, *MNRAS*, 302, 1
- Jones, P. A., Cunningham, M. R., Godfrey, P. D., & Cragg, D. M. 2007, *MNRAS*, 374, 579
- Koch, D., Toubin, C., Xu, S., Peslherbe, G., & Hynes, J. 2008, *J. Phys. Chem. C*, *in press* (DOI: 10.1021/jp076221+)
- Kuan, Y.-J., & Snyder, L. E. 1996, *ApJ*, 470, 981
- Kuan, Y.-J., Mehringer, D. M., & Snyder, L. E. 1996, *ApJ*, 459, 619
- Kuan, Y.-J., Charnley, S. B., Huang, H.-C., Tseng, W.-L., & Kisiel, Z. 2003, *ApJ*, 593, 848
- Lesaffre, P., Belloche, A., Chièze, J.-P., & André, P. 2005, *A&A*, 443, 961
- Lis, D. C., Carlstrom, J. E., & Keene, J. 1991, *ApJ*, 380, 429
- Lis, D. C., Goldsmith, P. F., Carlstrom, J. E., & Scoville, N. Z. 1993, *ApJ*, 402, 238
- Liu, S.-Y., & Snyder, L. E. 1999, *ApJ*, 523, 683
- Liu, S.-Y., Mehringer, D. M., & Snyder, L. E. 2001, *ApJ*, 552, 654
- MacDonald, J. N. & Tyler, J. K. 1972, *J. Chem. Soc. Chem. Comm.*, 995
- Maeda, S., & Ohno, K. 2006, *ApJ*, 640, 823
- Mehring, D. M., Palmer, P., & Goss, W. M. 1995, *ApJS*, 97, 497
- Mehring, D. M., & Menten, K. M. 1997, *ApJ*, 474, 346
- Mehring, D. M., Snyder, L. E., Miao, Y., & Lovas, F. J. 1997, *ApJ*, 480, L71
- Menten, K. M. 2004, in *The Dense Interstellar Medium in Galaxies*, Eds. Palfner, Kramer, Staubmeier, & Heithausen, Springer proceedings in physics, Vol. 91 (Berlin, Heidelberg: Springer), 69
- Miao, Y., Mehringer, D. M., Kuan, Y.-J., & Snyder, L. E. 1995, *ApJ*, 445, L59
- Miao, Y., & Snyder, L. E. 1997, *ApJ*, 480, L67
- Minh, Y. C., Irvine, W. M., & Friberg, P. 1992, *A&A*, 258, 489
- Morris, M., & Serabyn, E. 1996, *ARA&A*, 34, 645
- Müller, H. S. P., Thorwirth, S., Roth, D. A., & Winnewisser, G. 2001, *A&A*, 370, L49
- Müller, H. S. P., Schlöder, F., Stutzki, J., & Winnewisser, G. 2005, *J. Mol. Struct.*, 742, 215
- Muñoz Caro, G. M., Meierhenrich, U. J., Schutte, W. A., Barbier, B., et al. 2002, *Nature*, 416, 403
- Peltzer, E. T., Bada, J. L., Schlesinger, G., & Miller, S. L. 1984, *Advances in Space Research*, 4, 69
- Nummelin, A., Bergman, P., Hjalmarson, Å., Friberg, P., Irvine, W. M., Millar, T. J., Oishi, M., & Saito, S. 2000, *ApJS*, 128, 213
- Ossenkopf, V., & Henning, T. 1994, *A&A*, 291, 943
- Pickett, H. M. 1973, *J. Mol. Spectrosc.*, 46, 335
- Pickett, H. M. 1991, *J. Mol. Spectrosc.*, 148, 371
- Pickett, H. M., Poynter, R. L., Cohen, E. A., Delitsky, M. L., Pearson, J. C., & Müller, H. S. P. 1998, *J. Quant. Spectrosc. & Rad. Transfer*, 60, 883
- Pizzarello, S., & Huang, Y. 2005, *Geochim. Cosmochim. Acta*, 69, 599
- Reid, M. J. 1993, *ARA&A*, 31, 345
- Reid, M. J., Schneps, M. H., Moran, J. M., Gwinn, C. R., Genzel, R., Downes, D., & Roennaeng, B. 1988, *ApJ*, 330, 809
- Remijan, A., Snyder, L. E., Liu, S.-Y., Mehringer, D., & Kuan, Y.-J. 2002, *ApJ*, 576, 264
- Requena-Torres, M. A., Martín-Pintado, J., Rodríguez-Franco, A., Martín, S., Rodríguez-Fernández, N. J., & de Vicente, P. 2006, *A&A*, 455, 971
- Sault, R. J., Teuben, P. J., & Wright, M. C. H. 1995, *Astronomical Data Analysis Software and Systems IV*, 77, 433
- Snyder, L. E., Kuan, Y.-J., & Miao, Y. 1994, *Lecture Notes in Physics 439: The Structure and Content of Molecular Clouds*, Eds. T. L. Wilson and K. J. Johnston, Springer-Verlag, 439, 187
- Snyder, L. E., Lovas, F. J., Mehringer, D. M., Miao, N. Y., Kuan, Y., Hollis, J. M., & Jewell, P. R. 2002, *ApJ*, 578, 245
- Snyder, L. E., Lovas, F. J., Hollis, J. M., Friedel, D. N., et al. 2005, *ApJ*, 619, 914
- Storey, J. W. V. 1976, Ph.D. Thesis, Monash University
- Turner, B. E., & Apponi, A. J. 2001, *ApJ*, 561, L207
- Vogel, S. N., Genzel, R., & Palmer, P. 1987, *ApJ*, 316, 243
- Wirström, E. S., Bergman, P., Hjalmarson, Å., & Nummelin, A. 2007, *A&A*, 473, 177
- Woon, D. E. 2002, *ApJ*, 571, L177

List of Objects

- ‘Sagittarius B2’ on page 1
- ‘Sgr B2(M)’ on page 1
- ‘Sgr B2(N)’ on page 1
- ‘Orion KL’ on page 15
- ‘W51 e1/e2’ on page 15
- ‘S140’ on page 15
- ‘W3(OH)’ on page 15

Online Material

Table 2. Transitions of amino acetonitrile observed with the IRAM 30m telescope toward Sgr B2(N). The horizontal lines mark discontinuities in the observed frequency coverage. All lines with $S\mu^2 < 20 D^2$ are not listed, since they are expected to be much too weak to be detectable with our sensitivity.

N^a	Transition ^b	Frequency (MHz)	Unc. ^c (kHz)	E_l^d (K)	$S\mu^2$ (D^2)	σ^e (mK)	Comments
(1)	(2)	(3)	(4)	(5)	(6)	(7)	(8)
1	9 _{0,9} - 8 _{0,8}	80947.479	7	16	60	33	Detected
2	9 _{2,8} - 8 _{2,7}	81535.184	6	21	57	18	Strong HC ¹³ CCN, $v=0$
3	9 _{5,5} - 8 _{5,4} *	81700.966	6	47	41	13	Group detected , partial blend with U-line
5	9 _{6,3} - 8 _{6,2} *	81702.498	5	60	33	13	Group detected , partial blend with U-line
7	9 _{4,6} - 8 _{4,5} *	81709.838	6	35	48	13	Group detected
9	9 _{7,3} - 8 _{7,2}	81709.848	6	76	24	13	Group detected
10	9 _{4,5} - 8 _{4,4}	81710.098	6	35	48	13	Group detected
11	9 _{3,7} - 8 _{3,6}	81733.892	6	27	53	13	Detected , blend with CH ₃ OCH ₃ and HCC ¹³ CN, $v_6=1$
12	9 _{3,6} - 8 _{3,5}	81756.174	6	27	53	13	Detected , blend with U-line
13	9 _{2,7} - 8 _{2,6}	82224.644	7	21	57	19	Detected , uncertain baseline
14	9 _{1,8} - 8 _{1,7}	83480.894	8	17	59	17	Blend with C ₂ H ₃ CN, $v=0$
15	10 _{1,10} - 9 _{1,9}	88240.541	8	20	66	19	Strong HNCO, $v=0$ and HN ¹³ CO, $v=0$
16	10 _{0,10} - 9 _{0,9}	89770.285	7	19	66	18	Blend with U-line
17	10 _{2,9} - 9 _{2,8}	90561.332	6	25	64	20	Detected , blend with weak C ₂ H ₅ CN, $v_{13}=1/v_{21}=1$
18	10 _{6,4} - 9 _{6,3} *	90783.538	6	64	43	14	Group detected , partial blend with CH ₂ (OH)CHO and U-line
20	10 _{5,6} - 9 _{5,5} *	90784.281	6	50	50	14	Group detected , partial blend with CH ₂ (OH)CHO and U-line
22	10 _{7,3} - 9 _{7,2} *	90790.259	6	80	34	14	Group detected , blend with U-line
24	10 _{4,7} - 9 _{4,6}	90798.685	6	39	56	14	Group detected , blend with U-line
25	10 _{4,6} - 9 _{4,5}	90799.249	6	39	56	14	Group detected , blend with U-line
26	10 _{8,2} - 9 _{8,1} *	90801.896	7	98	24	14	Blend with U-line and HC ¹³ CCN, $v_7=1$
28	10 _{3,8} - 9 _{3,7}	90829.945	6	31	60	14	Detected , blend with U-line also in M?
29	10 _{3,7} - 9 _{3,6}	90868.038	6	31	60	14	Detected , partial blend with U-line
30	10 _{2,8} - 9 _{2,7}	91496.108	8	25	64	24	Detected , partial blend with CH ₃ CN, $v_4=1$ and U-line
31	10 _{1,9} - 9 _{1,8}	92700.172	8	21	66	28	Blend with U-line and CH ₃ OCH ₃
32	11 _{1,11} - 10 _{1,10}	97015.224	8	25	72	21	Detected , partial blend with C ₂ H ₅ OH and CH ₃ OCHO
33	11 _{0,11} - 10 _{0,10}	98548.363	8	24	73	18	Blend with C ₂ H ₅ CN, $v=0$
34	11 _{2,10} - 10 _{2,9}	99577.063	7	29	71	19	Blend with CH ₃ OCHO, $v_i=1$
35	11 _{6,6} - 10 _{6,5} *	99865.516	6	68	51	14	Strong blend with C ₂ H ₅ OH, CCS
37	11 _{5,7} - 10 _{5,6} *	99869.306	6	55	58	14	Strong CH ₃ OCHO, $v_i=1$
39	11 _{7,4} - 10 _{7,3} *	99871.151	6	84	43	14	Strong CH ₃ OCHO, $v_i=1$
41	11 _{8,3} - 10 _{8,2} *	99882.826	7	103	34	14	Strong blend with C ₂ H ₅ CN, $v_{13}=1/v_{21}=1$
43	11 _{4,8} - 10 _{4,7}	99890.599	6	44	63	14	Strong blend with HC ¹³ CCN, $v_7=1$ and HC ¹³ CCN, $v_6=1$
44	11 _{4,7} - 10 _{4,6}	99891.725	6	44	63	14	Strong blend with HC ¹³ CCN, $v_6=1$ and NH ₂ CN
45	11 _{9,2} - 10 _{9,1} *	99898.969	8	124	24	14	Strong HCC ¹³ CN, $v_6=1$
47	11 _{3,9} - 10 _{3,8}	99928.886	6	35	68	14	Detected , partial blend with NH ₂ CN and U-line
48	11 _{3,8} - 10 _{3,7}	99990.567	7	35	68	14	Detected
49	11 _{2,9} - 10 _{2,8}	100800.876	8	29	71	20	Detected , partial blend with CH ₃ CH ₃ CO, $v=0$ and U-line
50	11 _{1,10} - 10 _{1,9}	101899.795	8	26	72	34	Detected , uncertain baseline
51	12 _{1,12} - 11 _{1,11}	105777.991	8	29	79	43	Detected , blend with c-C ₂ H ₄ O and C ₂ H ₅ CN, $v=0$
52	12 _{0,12} - 11 _{0,11}	107283.142	8	29	80	24	Detected , blend with C ₂ H ₅ OH and U-line
53	12 _{2,11} - 11 _{2,10}	108581.408	7	34	77	20	Detected , weak blend with C ₂ H ₅ OH
54	12 _{6,7} - 11 _{6,6} *	108948.523	6	73	60	29	Blend with C ₂ H ₅ CN, $v=0$ and C ₂ H ₅ OH
56	12 _{7,5} - 11 _{7,4} *	108952.574	6	89	53	29	Blend with C ₂ H ₅ OH
58	12 _{5,8} - 11 _{5,7} *	108956.206	6	60	66	29	Group detected , blend with C ₂ H ₅ OH
60	12 _{8,4} - 11 _{8,3} *	108963.964	7	108	44	29	Strong blend with HC ¹³ CCN, $v_7=1$
62	12 _{9,3} - 11 _{9,2} *	108980.660	8	128	35	29	Strong blend with HCC ¹³ CN, $v_6=1$
64	12 _{4,9} - 11 _{4,8}	108985.821	6	48	71	29	Blend with HCC ¹³ CN, $v_7=1$
65	12 _{4,8} - 11 _{4,7}	108987.928	6	48	71	29	Blend with HCC ¹³ CN, $v_7=1$
66	12 _{10,2} - 11 _{10,1} *	109001.603	10	152	24	29	Weak
68	12 _{3,10} - 11 _{3,9}	109030.225	6	40	75	29	Detected , partial blend with HC ₃ N, $v_4=1$, C ₂ H ₅ OH, and U-line
69	12 _{3,9} - 11 _{3,8}	109125.734	7	40	75	29	Strong HC ¹³ CCN, $v_7=1$

(a) Numbering of the observed transitions with $S\mu^2 > 20 D^2$.

(b) Transitions marked with a * are double with a frequency difference less than 0.1 MHz. The quantum numbers of the second one are not shown.

(c) Frequency uncertainty.

(d) Lower energy level in temperature units (E_l/k_B).(e) Calculated rms noise level in T_{mb} scale.

Table 2. (continued)

N ^a	Transition ^b	Frequency (MHz)	Unc. ^c (kHz)	E _l ^d (K)	Sμ ² (D ²)	σ ^e (mK)	Comments (8)
(1)	(2)	(3)	(4)	(5)	(6)	(7)	(8)
70	12 _{2,10} - 11 _{2,9}	110136.314	8	34	77	24	Blend with ¹³ CH ₃ OH, v=0
71	12 _{1,11} - 11 _{1,10}	111076.901	8	31	79	25	Detected , slightly shifted?
72	13 _{1,13} - 12 _{1,12}	114528.654	8	34	86	37	Detected , partial blend with U-line
73	13 _{0,13} - 12 _{0,12}	115977.853	50	34	86	79	Blend with CH ₃ ¹³ CH ₂ CN, v=0, CH ₃ CH ₃ CO, and C ₂ H ₅ CN, v=0
74	15 _{7,9} - 14 _{7,8} *	136200.478	6	106	78	28	Strong HC ¹³ CCN, v ₇ =1
76	15 _{6,10} - 14 _{6,9} *	136204.641	5	90	84	28	Strong HC ¹³ CCN, v ₇ =1
78	15 _{8,7} - 14 _{8,6} *	136208.805	7	125	71	28	Strong HC ¹³ CCN, v ₇ =1 and HC ¹³ CCN, v ₆ =1
80	15 _{9,6} - 14 _{9,5} *	136225.653	8	145	64	28	Strong HCC ¹³ CN, v ₆ =1 and HCC ¹³ CN, v ₇ =1
82	15 _{5,11} - 14 _{5,10}	136229.823	5	77	89	28	Blend with HCC ¹³ CN, v ₇ =1
83	15 _{5,10} - 14 _{5,9}	136230.008	5	77	89	28	Blend with HCC ¹³ CN, v ₇ =1
84	15 _{10,5} - 14 _{10,4} *	136248.969	10	169	55	28	Group detected , blend with U-line
86	15 _{11,4} - 14 _{11,3} *	136277.600	13	195	46	28	Strong HC ₃ N, v ₄ =1 and CH ₃ OCHO
88	15 _{4,12} - 14 _{4,11}	136293.271	6	65	93	28	Strong CH ₃ ¹³ CH ₂ CN
89	15 _{4,11} - 14 _{4,10}	136303.599	6	65	93	28	Detected , blend with a(CH ₂ OH) ₂ and CH ₃ C ₃ N
90	15 _{12,3} - 14 _{12,2} *	136310.849	16	223	36	28	Weak, blend with CH ₃ C ₃ N
92	15 _{3,13} - 14 _{3,12}	136341.155	6	57	96	28	Detected , partial blend with U-line also in M
93	15 _{13,2} - 14 _{13,1} *	136348.271	21	253	25	28	Weak, blend with U-line
95	16 _{7,9} - 15 _{7,8} *	145284.487	30	113	86	25	Strong HC ¹³ CCN, v ₇ =1
97	16 _{8,8} - 15 _{8,7} *	145290.958	30	131	80	25	Blend with HC ¹³ CCN, v ₆ =1
99	16 _{6,11} - 15 _{6,10} *	145292.688	30	97	91	25	Blend with HC ¹³ CCN, v ₆ =1
101	16 _{9,7} - 15 _{9,6} *	145307.254	30	152	73	25	Strong C ₂ H ₅ CN, v ₁₃ =1/v ₂₁ =1, HCC ¹³ CN, v ₇ =1, C ₂ H ₃ CN, v ₁₅ =1
103	16 _{5,12} - 15 _{5,11}	145325.871	30	83	96	25	Group detected , uncertain baseline, partial blend with C ₂ H ₅ CN, v ₁₃ =1/v ₂₁ =1
104	16 _{5,11} - 15 _{5,10}	145326.209	30	83	96	25	Group detected , uncertain baseline, partial blend with C ₂ H ₅ CN, v ₁₃ =1/v ₂₁ =1
105	16 _{10,6} - 15 _{10,5} *	145330.985	40	175	65	25	Group detected , uncertain baseline
107	16 _{11,5} - 15 _{11,4} *	145360.684	30	201	56	25	Strong HC ₃ N, v ₄ =1
109	16 _{12,4} - 15 _{12,3} *	145395.485	60	229	46	25	Blend with C ₃ H ₇ CN
111	16 _{4,13} - 15 _{4,12}	145403.421	30	72	100	25	Blend with U-line or wing of C ₂ H ₅ CN, v=0
112	16 _{4,12} - 15 _{4,11}	145419.704	30	72	100	25	Strong C ₂ H ₅ CN, v=0
113	16 _{13,3} - 15 _{13,2} *	145434.928	60	260	36	25	Weak, blend with U-line
115	16 _{3,14} - 15 _{3,13}	145443.850	30	63	103	25	Detected , blend with C ₂ H ₅ CN, v=0 and U-line
116	16 _{14,2} - 15 _{14,1} *	145478.462	60	293	25	25	Weak, strong O ¹³ CS
118	16 _{1,15} - 15 _{1,14}	147495.789	6	55	106	31	Detected , partial blend with H ₃ C ¹³ CN, v ₈ =1
119	16 _{2,14} - 15 _{2,13}	147675.839	30	58	105	31	Blend with H ₃ C ¹³ CN, v ₈ =1, U-line, and CH ₃ OCHO
120	17 _{7,10} - 16 _{7,9} *	154369.232	40	120	94	112	Strong HC ¹³ CCN, v ₇ =1 and HC ¹³ CCN, v ₆ =1
122	17 _{8,9} - 16 _{8,8} *	154373.384	40	138	88	112	Strong HC ¹³ CCN, v ₆ =1
124	17 _{6,12} - 16 _{6,11} *	154382.222	40	104	99	112	Strong HCC ¹³ CN, v ₆ =1 and HCC ¹³ CN, v ₇ =1
126	17 _{9,8} - 16 _{9,7} *	154388.904	40	159	81	112	Strong HCC ¹³ CN, v ₇ =1
128	17 _{10,7} - 16 _{10,6} *	154412.758	50	182	74	112	Strong HNCO, v=0
130	17 _{5,13} - 16 _{5,12}	154424.604	40	90	103	112	Strong CH ₃ OH, v=0
131	17 _{5,12} - 16 _{5,11}	154425.216	40	90	103	112	Strong CH ₃ OH, v=0
132	17 _{11,6} - 16 _{11,5} *	154443.330	60	208	66	112	Strong HC ₃ N, v ₄ =1 and CH ₃ ¹³ CH ₂ CN
134	17 _{12,5} - 16 _{12,4} *	154479.566	15	236	57	112	Strong C ₂ H ₅ CN, v=0
136	17 _{4,14} - 16 _{4,13}	154517.470	5	79	107	112	Blend with C ₂ H ₅ CN, v ₁₃ =1/v ₂₁ =1
137	17 _{13,4} - 16 _{13,3} *	154520.861	19	267	47	112	Blend with C ₂ H ₅ CN, v ₁₃ =1/v ₂₁ =1
139	17 _{4,13} - 16 _{4,12}	154542.406	5	79	107	112	Group detected , blend with U-line
140	17 _{3,15} - 16 _{3,14}	154544.046	5	70	109	112	Group detected , blend with U-line
141	17 _{14,3} - 16 _{14,2} *	154566.773	25	300	36	112	Weak, strong U-line
143	17 _{15,2} - 16 _{15,1} *	154617.004	33	335	25	112	Weak, strong U-line and C ₂ H ₅ CN, v ₁₃ =1/v ₂₁ =1
145	18 _{7,12} - 17 _{7,11} *	163454.794	5	127	101	38	Group detected , partial blend with HC ¹³ CCN, v ₆ =1 and HCC ¹³ CN, v ₆ =1
147	18 _{8,10} - 17 _{8,9} *	163456.136	6	146	96	38	Group detected , partial blend with HC ¹³ CCN, v ₆ =1 and HCC ¹³ CN, v ₆ =1
149	18 _{9,9} - 17 _{9,8} *	163470.472	8	166	90	38	Group detected , partial blend with HCC ¹³ CN, v ₇ =1
151	18 _{6,13} - 17 _{6,12} *	163473.305	5	111	106	38	Group detected , partial blend with HCC ¹³ CN, v ₇ =1
153	18 _{10,8} - 17 _{10,7} *	163494.265	9	190	83	38	Strong CH ₃ ¹³ CH ₂ CN

Table 2. (continued)

N^a	Transition ^b	Frequency (MHz)	Unc. ^c (kHz)	E_l^d (K)	$S\mu^2$ (D ²)	σ^e (mK)	Comments
(1)	(2)	(3)	(4)	(5)	(6)	(7)	(8)
155	18 _{11,7} - 17 _{11,6} *	163525.533	11	216	75	38	Group detected , blend with HC ₃ N, $v_4=1$
157	18 _{5,14} - 17 _{5,13}	163526.183	4	97	110	38	Group detected , blend with HC ₃ N, $v_4=1$
158	18 _{5,13} - 17 _{5,12}	163527.171	4	97	110	38	Group detected , blend with HC ₃ N, $v_4=1$
159	18 _{12,6} - 17 _{12,5} *	163563.084	14	244	66	38	Blend with C ₂ H ₃ CN, $v_{15}=2$ and SO ₂ , $v=0$
161	18 _{13,5} - 17 _{13,4} *	163606.161	18	274	57	38	Strong SO ₂ , $v=0$
163	18 _{4,15} - 17 _{4,14}	163635.326	5	86	114	38	Detected , partial blend with C ₃ H ₇ CN
164	18 _{3,16} - 17 _{3,15}	163640.468	5	78	116	38	Detected , partial blend with C ₃ H ₇ CN
165	18 _{14,4} - 17 _{14,3} *	163654.261	24	307	47	38	Weak, blend with H ¹³ CONH ₂ , $v=0$
167	18 _{4,14} - 17 _{4,13}	163672.524	5	86	114	38	Strong C ₂ H ₃ CN, $v_{13}=1/v_{21}=1$
168	18 _{15,3} - 17 _{15,2} *	163707.031	32	343	37	38	Weak, blend with CH ₂ (OH)CHO
170	18 _{2,16} - 17 _{2,15}	166463.884	30	72	118	66	Blend with ¹³ CH ₂ CHCN
171	19 _{8,12} - 18 _{8,11} *	172539.195	40	153	104	44	Strong HCC ¹³ CN, $v_6=1$
173	19 _{7,13} - 18 _{7,12} *	172541.207	40	135	109	44	Strong HCC ¹³ CN, $v_6=1$
175	19 _{9,10} - 18 _{9,9} *	172552.010	40	174	98	44	Strong HCC ¹³ CN, $v_7=1$
177	19 _{6,14} - 18 _{6,13} *	172566.092	50	119	114	44	Group detected , partial blend with U-line and HCC ¹³ CN, $v_7=1$
179	19 _{10,9} - 18 _{10,8} *	172575.485	50	198	91	44	Strong U-line
181	19 _{11,8} - 18 _{11,7} *	172607.260	60	223	84	44	Strong HC ₃ N, $v_4=1$
183	19 _{5,15} - 18 _{5,14}	172630.750	30	105	117	44	Strong U-line and t-HCOOH
184	19 _{5,14} - 18 _{5,13}	172632.382	30	105	117	44	Strong U-line and t-HCOOH
185	19 _{12,7} - 18 _{12,6} *	172645.994	13	252	76	44	Blend with t-HCOOH, H ¹³ CN, and U-line
187	19 _{13,6} - 18 _{13,5} *	172690.745	17	282	67	44	Strong H ¹³ CN and CH ₃ OCHO
189	19 _{3,17} - 18 _{3,16}	172731.699	30	86	123	44	Blend with U-line and C ₂ H ₃ CN, $v=0$
190	19 _{14,5} - 18 _{14,4} *	172740.945	23	315	58	44	Strong C ₂ H ₃ CN, $v=0$
192	19 _{4,16} - 18 _{4,15}	172756.821	30	94	121	44	Baseline problem?
193	19 _{15,4} - 18 _{15,3} *	172796.183	30	351	48	44	Weak, strong HCC ¹³ CN, $v_7=1$
195	19 _{4,15} - 18 _{4,14}	172811.041	30	94	121	44	Strong C ₂ H ₃ CN, $v=0$
196	19 _{16,3} - 18 _{16,2} *	172856.161	40	388	37	44	Weak, strong HC ₃ N, $v=0$ and HC ₃ N, $v_5=1/v_7=3$
198	20 _{0,20} - 19 _{0,19}	176174.096	30	81	132	365	Noisy, partial blend with HNCO, $v_5=1$ and U-line
199	23 _{0,23} - 22 _{0,22}	201875.876	10	108	152	138	Strong ¹³ CH ₃ CH ₂ CN, $v=0$
200	22 _{2,20} - 21 _{2,19}	203812.341	10	107	145	364	Strong C ₂ H ₃ CN, $v=0$
201	23 _{2,22} - 22 _{2,21}	206652.454	9	115	151	106	Blend with C ₂ H ₃ CN, $v=0$
202	23 _{8,16} - 22 _{8,15} *	208875.040	8	189	134	160	Blend with HCC ¹³ CN, $v_7=1$, CH ₃ CH ₃ CO, $v_t=1$, and CH ₃ OCHO
204	23 _{9,14} - 22 _{9,13} *	208877.860	9	210	129	160	Blend with HCC ¹³ CN, $v_7=1$, CH ₃ CH ₃ CO, $v_t=1$, and CH ₃ OCHO
206	23 _{7,17} - 22 _{7,16} *	208896.163	7	171	139	160	Strong C ₂ H ₃ CN, $v=0$
208	23 _{10,13} - 22 _{10,12} *	208897.241	10	233	124	160	Strong C ₂ H ₃ CN, $v=0$
210	23 _{11,12} - 22 _{11,11} *	208929.064	10	259	118	160	Strong C ₂ H ₃ CN, $v=0$
212	23 _{6,18} - 22 _{6,17}	208955.555	6	155	142	160	Blend with C ₂ H ₃ CN, $v=0$ and U-line
213	23 _{6,17} - 22 _{6,16}	208955.797	6	155	142	160	Blend with C ₂ H ₃ CN, $v=0$ and U-line
214	23 _{12,11} - 22 _{12,10} *	208970.868	11	287	111	160	Strong C ₂ H ₃ CN, $v=0$
216	23 _{3,21} - 22 _{3,20}	209015.508	7	121	150	160	Strong C ₂ H ₃ CN, $v=0$ and C ₂ H ₃ CN, $v=0$
217	23 _{13,10} - 22 _{13,9} *	209021.101	13	318	104	160	Strong C ₂ H ₃ CN, $v=0$
219	23 _{14,9} - 22 _{14,8} *	209078.736	16	351	96	160	Strong C ₂ H ₃ CN, $v=0$
221	23 _{5,19} - 22 _{5,18}	209081.032	6	141	146	160	Strong C ₂ H ₃ CN, $v=0$
222	23 _{5,18} - 22 _{5,17}	209090.124	6	141	146	160	Strong C ₂ H ₃ CN, $v=0$
223	23 _{15,8} - 22 _{15,7} *	209143.066	23	386	88	160	Weak, strong HC ¹³ CCN, $v_7=1$
225	23 _{16,7} - 22 _{16,6} *	209213.584	33	424	79	58	Weak, strong H ₂ CS and C ₂ H ₃ CN, $v_{15}=1$
227	23 _{4,20} - 22 _{4,19}	209272.189	6	130	148	58	Detected , blend CH ₃ CH ₃ CO, $v=0$
228	23 _{17,6} - 22 _{17,5} *	209289.914	46	464	69	58	Weak, blend with C ₂ H ₃ CN, $v_{13}=1/v_{21}=1$ and C ₂ H ₃ CN, $v_{15}=1$
230	23 _{18,5} - 22 _{18,4} *	209371.766	64	507	59	58	Weak, blend with C ₂ H ₅ OH
232	23 _{19,4} - 22 _{19,3} *	209458.910	86	552	49	58	Weak, strong C ₂ H ₃ CN, $v_{15}=2$ and C ₂ H ₅ CN, $v=0$
234	23 _{4,19} - 22 _{4,18}	209473.790	7	130	148	58	Strong C ₂ H ₃ CN, $v_{15}=2$ and CH ₃ OCHO
235	23 _{20,3} - 22 _{20,2} *	209551.156	114	599	37	58	Weak, strong C ₂ H ₃ CN, $v_{11}=1$
237	23 _{1,22} - 22 _{1,21}	209629.913	9	113	152	45	Detected , blend with HC ¹³ CCN, $v_7=2$ and HCC ¹³ CN, $v_7=2$
238	23 _{21,2} - 22 _{21,1} *	209648.342	146	649	25	45	Weak, blend with U-line and C ₂ H ₃ CN, $v_{11}=1$
240	24 _{1,24} - 23 _{1,23}	210072.793	12	118	159	45	Blend with C ₂ H ₅ CN, $v_{13}=1/v_{21}=1$ and ¹³ CH ₃ CH ₂ CN, $v=0$
241	24 _{0,24} - 23 _{0,23}	210448.044	12	118	159	64	Strong CH ₃ OCHO
242	23 _{3,20} - 22 _{3,19}	211099.150	12	122	150	33	Blend with U-lines

Table 2. (continued)

N ^a	Transition ^b	Frequency (MHz)	Unc. ^c (kHz)	E _l ^d (K)	Sμ ² (D ²)	σ ^e (mK)	Comments (8)
(1)	(2)	(3)	(4)	(5)	(6)	(7)	(8)
243	23 _{2,21} - 22 _{2,20}	213074.653	70	117	152	48	Strong SO ₂ , v=0
244	24 _{2,23} - 23 _{2,22}	215466.138	10	124	158	74	Strong C ₂ H ₅ CN, v ₁₃ =1/v ₂₁ =1
245	24 _{3,21} - 23 _{3,20}	220537.064	14	132	157	98	Strong CH ₃ CN, v ₈ =0
246	25 _{1,24} - 24 _{1,23}	226957.428	40	134	165	96	Strong CN absorption
247	25 _{9,16} - 24 _{9,15} *	227040.487	50	230	145	96	Group detected , partial blend with CN absorption and CH ₃ CH ₃ CO, v _t =1
249	25 _{8,18} - 24 _{8,17} *	227045.287	50	210	149	96	Group detected , partial blend with CN absorption and CH ₃ CH ₃ CO, v _t =1
251	25 _{10,15} - 24 _{10,14} *	227055.944	50	254	139	96	Group detected , partial blend with CN absorption
253	25 _{7,19} - 24 _{7,18} *	227079.847	50	191	153	96	Group detected , blend with CH ₂ CH ¹³ CN and CH ₃ OH, v=0
255	25 _{11,14} - 24 _{11,13} *	227086.424	50	280	134	96	Blend with CH ₂ CH ¹³ CN and CH ₃ OH, v=0
257	25 _{3,23} - 24 _{3,22}	227088.938	40	142	164	96	Blend with CH ₂ CH ¹³ CN and CH ₃ OH, v=0
258	25 _{12,13} - 24 _{12,12} *	227128.728	60	308	128	96	Blend with C ₂ H ₅ CN, v=0 and C ₂ H ₃ CN, v=0
260	25 _{17,8} - 24 _{17,7} *	227467.235	45	485	89	85	Weak, blend with CH ₂ (OH)CHO, CH ₂ CH ¹³ CN and t-C ₂ H ₅ OCHO
262	25 _{4,22} - 24 _{4,21}	227539.318	40	151	162	85	Strong HCONH ₂ , v ₁₂ =1 and C ₂ H ₅ CN, v=0
263	25 _{18,7} - 24 _{18,6} *	227555.295	63	528	80	85	Weak, strong CH ₃ OCHO
265	26 _{0,26} - 25 _{0,25}	227601.595	16	138	172	85	Strong HCONH ₂ , v=0
266	25 _{19,6} - 24 _{19,5} *	227649.239	85	572	70	85	Weak, blend with CH ₃ OCH ₃
268	25 _{20,5} - 24 _{20,4} *	227748.834	113	620	60	85	Weak, blend with ¹³ CH ₃ CH ₂ CN, v=0
270	25 _{21,4} - 24 _{21,3} *	227853.885	147	669	49	85	Weak, strong HC ¹³ CCN, v ₇ =2 and HCC ¹³ CN, v ₇ =2
272	25 _{4,21} - 24 _{4,20}	227892.614	60	151	162	85	Strong HCC ¹³ CN, v ₇ =2, C ₂ H ₅ OH, and HC ¹³ CCN, v ₇ =2
273	25 _{2,23} - 24 _{2,22}	231485.527	50	138	165	40	Detected , blend with U-line?
274	26 _{1,25} - 25 _{1,24}	235562.532	50	145	172	131	Strong C ₂ H ₃ CN, v=0
275	27 _{1,27} - 26 _{1,26}	235964.814	19	149	179	131	Strong ¹³ CH ₃ OH, v=0
276	26 _{3,24} - 25 _{3,23}	236103.949	40	153	170	37	Blend with HCC ¹³ CN, v ₇ =1 and C ₂ H ₅ CN, v ₁₃ =1/v ₂₁ =1
277	26 _{9,17} - 25 _{9,16} *	236121.689	50	241	152	37	Blend with ¹³ CH ₃ CH ₂ CN
279	26 _{8,19} - 25 _{8,18} *	236131.044	50	220	156	37	Blend with CH ₂ ¹³ CHCN
281	26 _{10,16} - 25 _{10,15} *	236134.730	50	265	147	37	Blend with CH ₂ ¹³ CHCN
283	26 _{11,15} - 25 _{11,14} *	236164.129	60	291	142	37	Strong C ₂ H ₃ CN, v ₁₁ =1 and ¹³ CH ₃ CH ₂ CN, v=0
285	26 _{7,20} - 25 _{7,19} *	236173.437	60	202	160	37	Blend with C ₂ H ₃ CN, v ₁₁ =1, CH ₂ ¹³ CHCN, and ¹³ CH ₃ CH ₂ CN, v=0
287	27 _{0,27} - 26 _{0,26}	236182.602	18	149	179	37	Blend with CH ₂ ¹³ CHCN, ¹³ CH ₃ CH ₂ CN, v=0, and HC ₃ N, v ₄ =1
288	26 _{12,14} - 25 _{12,13} *	236206.427	19	319	136	37	Strong SO ₂ , v=0
290	26 _{13,13} - 25 _{13,12} *	236259.339	21	349	130	37	Blend with C ₂ H ₅ CN, v ₁₃ =1/v ₂₁ =1 and t-C ₂ H ₅ OCHO
292	26 _{6,21} - 25 _{6,20}	236269.491	60	186	163	37	Group detected , partial blend with t-C ₂ H ₅ OCHO and U-line
293	26 _{6,20} - 25 _{6,19}	236270.459	60	186	163	37	Group detected , partial blend with t-C ₂ H ₅ OCHO and U-line
294	26 _{14,12} - 25 _{14,11} *	236321.411	23	382	123	37	Weak, blend with C ₂ H ₅ OH and CH ₃ ¹³ CH ₂ CN, v=0
296	26 _{15,11} - 25 _{15,10} *	236391.638	27	418	115	37	Weak, blend with CH ₂ ¹³ CHCN
298	26 _{5,22} - 25 _{5,21}	236454.502	40	173	166	37	Blend with SO, v=0 and ¹³ CH ₃ CH ₂ CN, v=0, baseline problem?
299	26 _{16,10} - 25 _{16,9} *	236469.303	35	456	107	37	Weak, blend with CH ₂ CH ¹³ CN
301	26 _{5,21} - 25 _{5,20}	236481.643	40	173	166	37	Blend with CH ₂ ¹³ CHCN
302	26 _{17,9} - 25 _{17,8} *	236553.897	80	496	99	37	Weak, blend with t-C ₂ H ₅ OCHO, ¹³ CH ₃ CH ₂ CN, v=0, and CH ₃ COOH, v _t =0
304	27 _{1,26} - 26 _{1,25}	244135.969	14	156	178	46	Blend with C ₂ H ₅ CN, v ₁₃ =1/v ₂₁ =1
305	28 _{1,28} - 27 _{1,27}	244585.841	21	161	186	39	Strong CH ₃ OCHO and HCC ¹³ CN, v=0
306	28 _{0,28} - 27 _{0,27}	244765.968	21	160	186	39	Detected , blend with CH ₃ ¹³ CH ₂ CN, v=0 and U-line
307	27 _{3,25} - 26 _{3,24}	245102.984	11	164	177	72	Blend with ¹³ CH ₃ CH ₂ CN, v=0
308	27 _{9,18} - 26 _{9,17} *	245202.855	16	253	159	72	Blend with ¹³ CH ₃ CH ₂ CN, v=0 and U-line?
310	27 _{10,17} - 26 _{10,16} *	245213.055	19	276	155	72	Strong CH ₃ OH, v=0
312	27 _{8,20} - 26 _{8,19} *	245217.230	13	232	164	72	Strong CH ₃ OH, v=0
314	27 _{11,16} - 26 _{11,15} *	245241.163	21	302	150	72	Blend with C ₂ H ₅ ¹³ CN, v=0 and C ₂ H ₃ CN, v ₁₅ =1
316	27 _{7,21} - 26 _{7,20} *	245268.168	11	213	167	72	Blend with HC ₃ N, v ₄ =1
318	27 _{12,15} - 26 _{12,14} *	245283.214	24	330	144	72	Blend with C ₂ H ₅ ¹³ CN, v=0
320	27 _{13,14} - 26 _{13,13} *	245336.715	26	361	138	72	Strong SO ₂ , v=0
322	27 _{6,22} - 26 _{6,21}	245378.722	10	197	170	72	Group detected , blend with ¹³ CH ₃ CH ₂ CN, v=0?
323	27 _{6,21} - 26 _{6,20}	245380.146	10	197	170	72	Group detected , blend with ¹³ CH ₃ CH ₂ CN, v=0?

Table 2. (continued)

N ^a	Transition ^b	Frequency (MHz)	Unc. ^c (kHz)	E _l ^d (K)	S μ ² (D ²)	σ ^e (mK)	Comments
(1)	(2)	(3)	(4)	(5)	(6)	(7)	(8)
324	27 _{14,13} - 26 _{14,12} *	245400.026	29	394	131	72	Blend with U-line, CH ₃ CH ₃ CO, v=0 and ¹³ CH ₃ CH ₂ CN, v=0?
326	27 _{15,12} - 26 _{15,11} *	245472.024	33	429	124	72	Weak, strong C ₂ H ₅ CN, v ₁₃ =1/v ₂₁ =1 and C ₂ H ₃ CN, v ₁₁ =1
328	27 _{16,11} - 26 _{16,10} *	245551.911	40	467	116	53	Weak, blend with SO ₂ , v=0
330	27 _{5,23} - 26 _{5,22}	245585.766	10	184	173	53	Strong CH ₂ ¹³ CHCN and HC ₃ N, v=0
331	27 _{5,22} - 26 _{5,21}	245623.711	10	184	173	53	Strong HC ₃ N, v ₅ =1/v ₇ =3 and CH ₂ ¹³ CHCN
332	27 _{17,10} - 26 _{17,9} *	245639.099	51	507	108	53	Weak, blend with C ₂ H ₃ CN, v ₁₅ =2
334	27 _{18,9} - 26 _{18,8} *	245733.144	67	550	100	53	Weak, strong HNCO, v ₅ =1
336	27 _{4,24} - 26 _{4,23}	245803.548	10	173	175	53	Blend with CH ₂ CH ¹³ CN
337	27 _{19,8} - 26 _{19,7} *	245833.697	88	595	91	53	Weak, strong U-line, partial blend with CH ₂ CH ¹³ CN and C ₂ H ₃ CN, v ₁₁ =1/v ₁₅ =1
339	27 _{20,7} - 26 _{20,6} *	245940.476	116	642	81	53	Weak, strong U-line and CH ₃ OCHO, v _i =1
341	27 _{21,6} - 26 _{21,5} *	246053.247	150	692	71	53	Weak, strong CH ₃ OCHO
343	28 _{3,26} - 27 _{3,25}	254085.051	12	176	184	32	Blend with CH ₃ CH ₃ CO, v=0 and C ₂ H ₅ CN, v=0
344	28 _{9,19} - 27 _{9,18} *	254283.930	19	264	167	32	Strong SO ₂ , v=0 and ¹³ CH ₃ OH, v=0
346	28 _{10,18} - 27 _{10,17} *	254290.939	22	288	162	32	Strong SO ₂ , v=0, ¹³ CH ₃ OH, v=0, ¹³ CH ₂ CHCN, ¹³ CH ₃ CH ₂ CN, v=0, and H ¹³ CONH ₂ , v ₁₂ =1
348	28 _{8,21} - 27 _{8,20} *	254303.873	15	244	171	32	Blend with ¹³ CH ₃ CH ₂ CN, v=0 and C ₂ H ₅ CN, v=0
350	28 _{11,17} - 27 _{11,16} *	254317.460	26	314	157	32	Strong C ₂ H ₅ CN, v=0 and ¹³ CH ₃ OH, v=0
352	28 _{12,16} - 27 _{12,15} *	254359.074	29	342	152	32	Blend with H ¹³ CONH ₂ , v=0
354	28 _{7,22} - 27 _{7,21} *	254364.160	12	225	174	32	Blend with H ¹³ CONH ₂ , v=0
356	28 _{13,15} - 27 _{13,14} *	254413.004	32	372	146	32	Strong C ₂ H ₅ CN, v=0, H ¹³ CONH ₂ , v=0, and CH ₃ OH, v=0
358	28 _{22,6} - 27 _{22,5} *	255273.081	196	755	71	217	Weak, strong ¹³ CH ₃ OH, v=0 and CH ₂ CH ¹³ CN
360	28 _{23,5} - 27 _{23,4} *	255401.564	245	809	60	217	Weak, blend with CH ₃ CH ₃ CO, v _i =1
362	28 _{24,4} - 27 _{24,3} *	255535.733	304	866	49	217	Weak, blend with SO ₂ , v=0 and U-line?
364	28 _{4,24} - 27 _{4,23}	255674.369	18	185	182	217	Strong HC ₃ N, v ₇ =1
365	28 _{25,3} - 27 _{25,2} *	255675.432	372	925	38	217	Strong HC ₃ N, v ₇ =1
367	28 _{2,26} - 27 _{2,25}	258775.885	19	172	185	1609	Weak, blend with CH ₃ OH, v=0
368	29 _{9,20} - 28 _{9,19} *	263364.923	22	277	174	74	Group detected , baseline problem?, blend with U-line
370	29 _{10,19} - 28 _{10,18} *	263368.355	26	300	170	74	Group detected , baseline problem?, blend with U-line
372	29 _{8,22} - 28 _{8,21} *	263390.982	17	256	178	74	Blend with HNCO, v ₄ =1 and CH ₃ OCH ₃
374	29 _{11,18} - 28 _{11,17} *	263393.008	31	326	165	74	Blend with HNCO, v ₄ =1 and CH ₃ OCH ₃
376	29 _{12,17} - 28 _{12,16} *	263433.971	35	354	160	74	Strong HC ₃ N, v ₄ =1, HNCO, v ₅ =1, and HNCO, v=0
378	29 _{7,23} - 28 _{7,22} *	263461.436	14	237	181	74	Blend with HNCO, v=0, CH ₃ CH ₃ CO, v=0 and C ₂ H ₅ OH
380	29 _{13,16} - 28 _{13,15} *	263488.164	40	385	154	74	Blend with C ₂ H ₅ ¹³ CN, v=0
382	29 _{14,15} - 28 _{14,14} *	263553.566	44	418	148	74	Strong SO ₂ , v=0, HCONH ₂ , v ₁₂ =1, and CH ₂ (OH)CHO
384	29 _{6,24} - 28 _{6,23}	263604.573	12	221	184	74	Group detected , baseline problem?, partial blend with CH ₃ CH ₃ CO, v _i =1 and CH ₃ OCH ₃
385	29 _{6,23} - 28 _{6,22}	263607.689	12	221	184	74	Group detected , baseline problem?, partial blend with CH ₃ CH ₃ CO, v _i =1 and CH ₃ OCH ₃
386	29 _{15,14} - 28 _{15,13} *	263628.792	50	453	141	74	Strong CH ₃ OCH ₃
388	29 _{16,13} - 28 _{16,12} *	263712.865	57	491	134	108	Weak, strong HCC ¹³ CN, v ₇ =1 and HNCO, v ₆ =1
390	29 _{17,12} - 28 _{17,11} *	263805.068	67	531	126	108	Weak, strong HC ₃ N, v ₅ =1/v ₇ =3 and C ₂ H ₅ CN, v=0
392	29 _{5,25} - 28 _{5,24}	263857.842	12	208	187	108	Blend with HCONH ₂ , v=0 and C ₂ H ₅ ¹³ CN, v=0
393	29 _{18,11} - 28 _{18,10} *	263904.858	81	574	118	108	Weak, blend with SO ₂ , v=0, C ₂ H ₅ CN, v ₁₃ =1/v ₂₁ =1, and U-line?
395	29 _{5,24} - 28 _{5,23}	263928.994	13	208	187	108	Blend with C ₂ H ₅ CN, v ₁₃ =1/v ₂₁ =1 and C ₂ H ₅ CN, v=0
396	29 _{19,10} - 28 _{19,9} *	264011.816	101	619	110	108	Weak, strong CH ₃ ¹³ CH ₂ CN, v=0
398	29 _{4,26} - 28 _{4,25}	264055.836	13	197	189	108	Detected , partial blend with C ₂ H ₅ CN, v=0 and CH ₃ CH ₃ CO, v=0

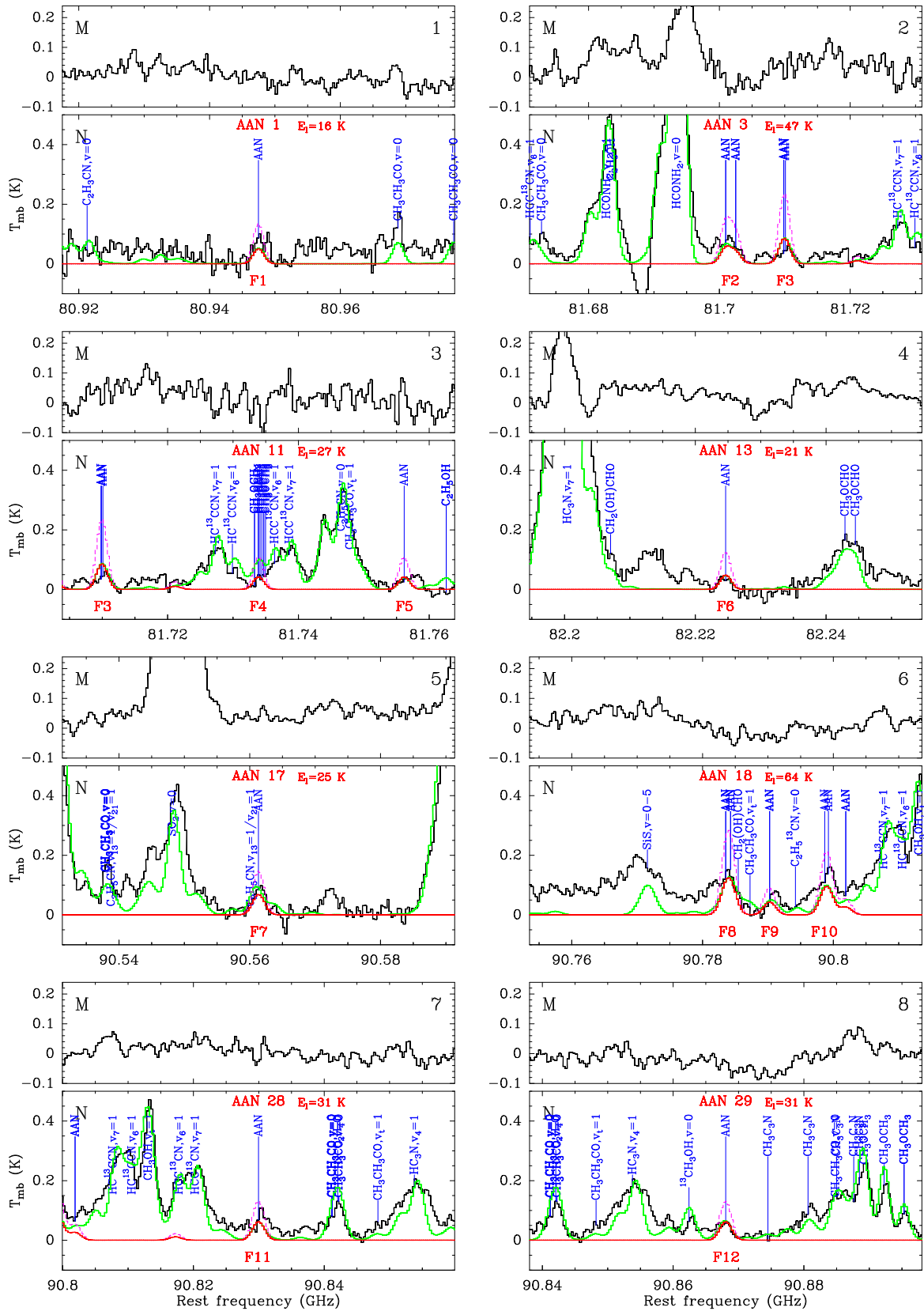


Fig. 1. Transitions of amino acetonitrile (AAN) detected with the IRAM 30m telescope. Each panel consists of two plots and is labeled in black in the upper right corner. The lower plot shows in black the spectrum obtained toward Sgr B2(N) in main-beam temperature scale (K), while the upper plot shows the spectrum toward Sgr B2(M). The rest frequency axis is labeled in GHz. The systemic velocities assumed for Sgr B2(N) and (M) are 64 and 62 km s⁻¹, respectively. The lines identified in the Sgr B2(N) spectrum are labeled in blue. The top red label indicates the AAN transition centered in each plot (numbered like in col. 1 of Table 3), along with the energy of its lower level in K (E_l/k_B). The other AAN lines are labeled in blue only. The bottom red label is the feature number (see col. 8 of Table 3). The green spectrum shows our LTE model containing all identified molecules, including AAN. The LTE synthetic spectrum of AAN alone is overlaid in red, and its opacity in dashed violet. All observed lines which have no counterpart in the green spectrum are still unidentified in Sgr B2(N).

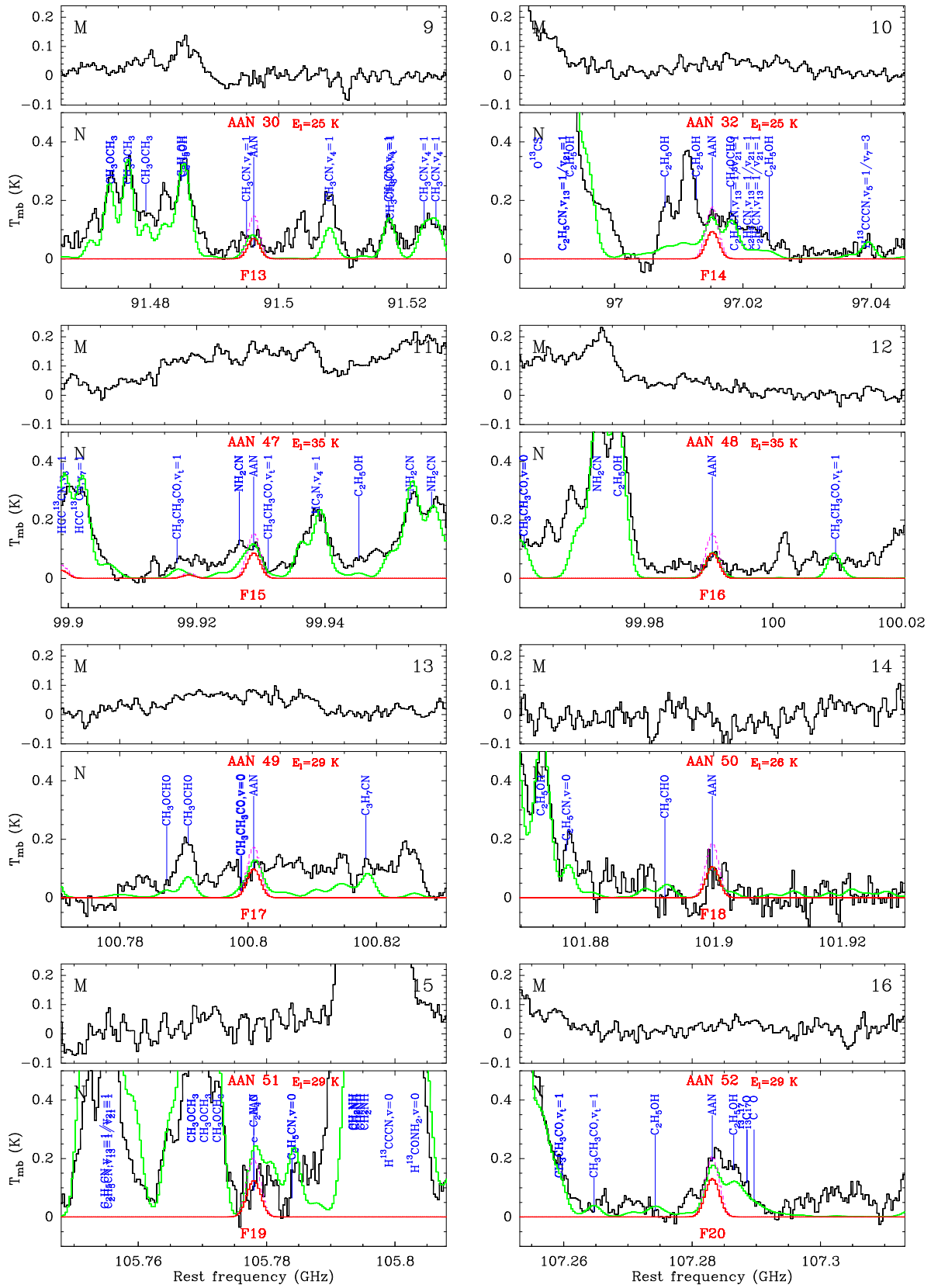


Fig. 1. (continued)

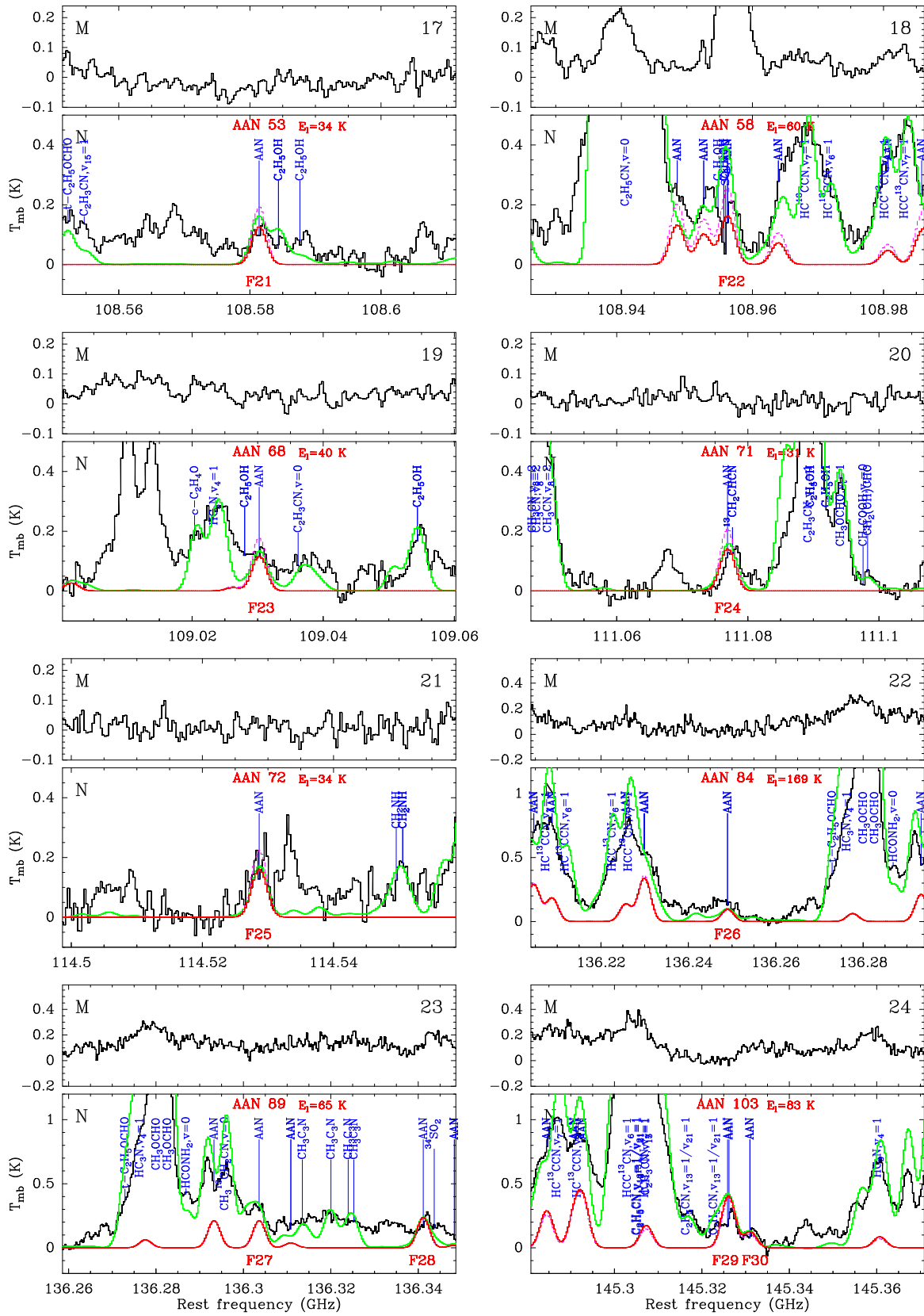


Fig. 1. (continued)

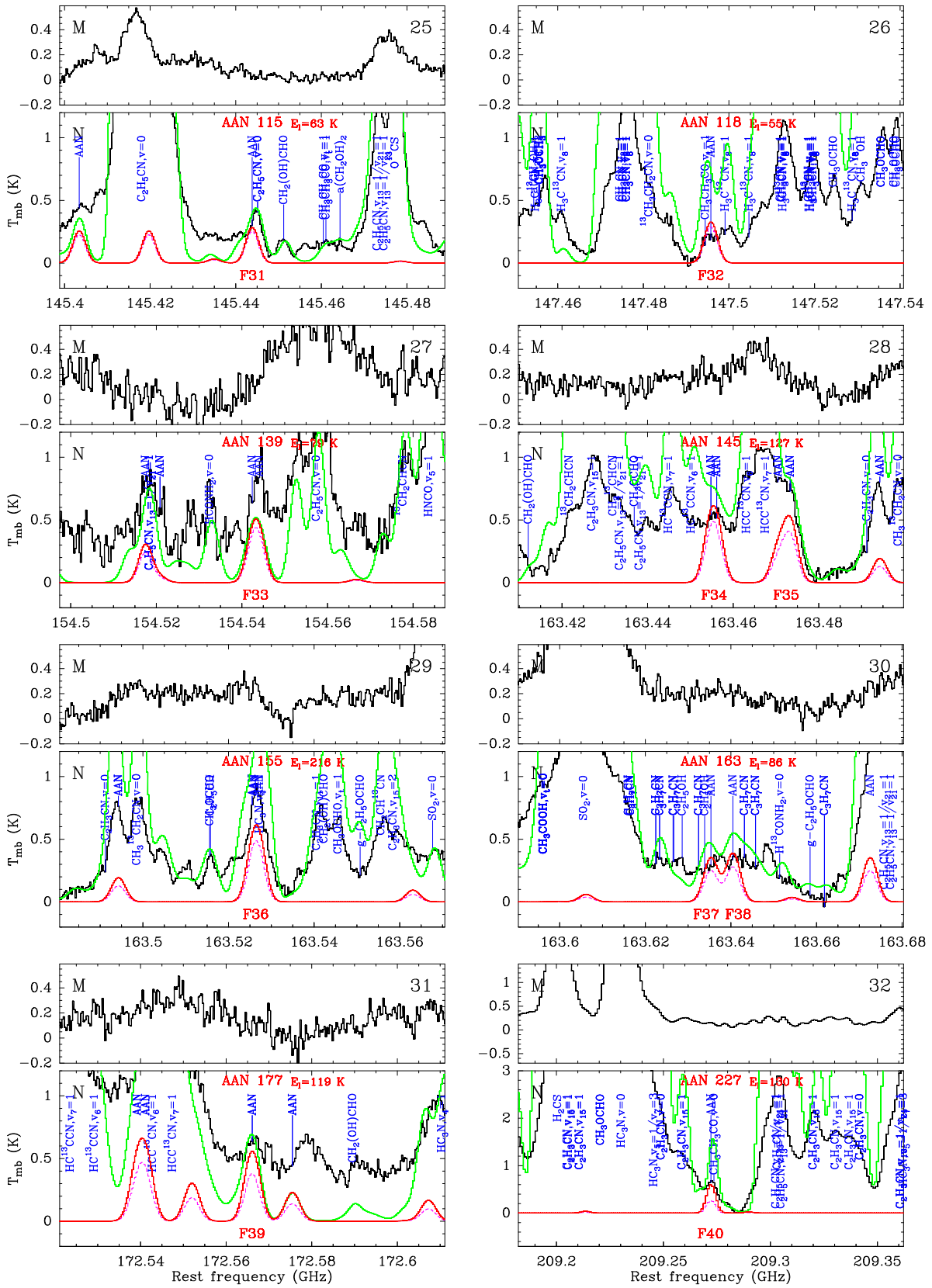


Fig. 1. (continued)

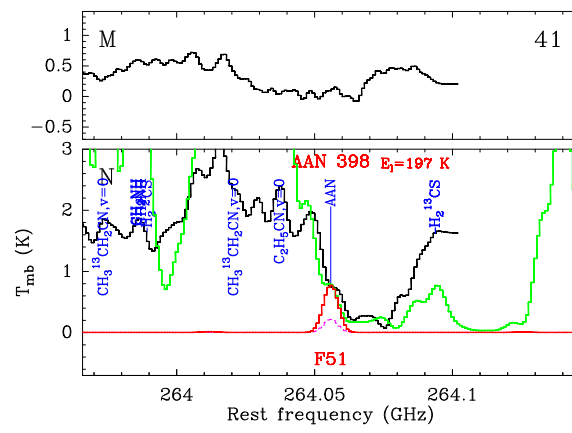


Fig. 1. (continued)